Monthly Notices
of the
ROYAL ASTRONOMICAL SOCIETY

MNRAS **439,** 446–473 (2014) doi:10.1093/mnras/stu023
Advance Access publication 2014 February 6

Galactic winds and stellar populations in Lyman α emitting galaxies at $z \sim 3.1$

E. M. McLinden,[1]⋆ J. E. Rhoads,[2] S. Malhotra,[2] S. L. Finkelstein,[3]
M. L. A. Richardson,[2] B. Smith[2] and V. S. Tilvi[4]

[1]*McDonald Observatory, The University of Texas at Austin, Austin, TX 78712, USA*
[2]*School of Earth and Space Exploration, Arizona State University, Tempe, AZ 85287, USA*
[3]*Department of Astronomy, The University of Texas at Austin, Austin, TX 78712, USA*
[4]*George P. and Cynthia Woods Mitchell Institute for Fundamental Physics and Astronomy, and Department of Physics and Astronomy, Texas A&M University, College Station, TX 77843, USA*

Accepted 2013 December 19. Received 2013 December 16; in original form 2013 October 21

ABSTRACT

We present a sample of 33 spectroscopically confirmed $z \sim 3.1$ Lyα-emitting galaxies (LAEs) in the Cosmological Evolution Survey (COSMOS) field. This paper details the narrow-band survey we conducted to detect the LAE sample, the optical spectroscopy we performed to confirm the nature of these LAEs, and a new near-infrared spectroscopic detection of the [O III] 5007 Å line in one of these LAEs. This detection is in addition to two [O III] detections in two $z \sim 3.1$ LAEs we have reported on previously McLinden et al. The bulk of the paper then presents detailed constraints on the physical characteristics of the entire LAE sample from spectral energy distribution (SED) fitting. These characteristics include mass, age, star-formation history, dust content, and metallicity. We also detail an approach to account for nebular emission lines in the SED fitting process – wherein our models predict the strength of the [O III] line in an LAE spectrum. We are able to study the success of this prediction because we can compare the model predictions to our actual near-infrared observations both in galaxies that have [O III] detections and those that yielded non-detections. We find a median stellar mass of 6.9×10^8 M$_\odot$ and a median star formation rate weighted stellar population age of 4.5×10^6 yr. In addition to SED fitting, we quantify the velocity offset between the [O III] and Lyα lines in the galaxy with the new [O III] detection, finding that the Lyα line is shifted 52 km s^{-1} redwards of the [O III] line, which defines the systemic velocity of the galaxy.

Key words: galaxies: high-redshift.

1 INTRODUCTION

High-redshift Lyman α emitting galaxies (LAEs) are now routinely identified via narrow-band (NB) detection methods (e.g. Cowie & Hu 1998; Malhotra & Rhoads 2002, 2004; Ouchi et al. 2003; Gawiser et al. 2006). Now that samples of these galaxies can be more easily compiled at a variety of redshifts, attention has turned to deriving the physical characteristics of these galaxies by fitting spectral energy distributions (SEDs) to their observed photometry of these galaxies (Gawiser et al. 2006, 2007; Finkelstein et al. 2007, 2008, 2009, 2011a; Lai et al. 2007, 2008; Nilsson et al. 2007, 2011; Pirzkal et al. 2007; Ono et al. 2010; Acquaviva et al. 2012).

The majority of early work in SED fitting (e.g. Gawiser et al. 2006; Finkelstein et al. 2007; Nilsson et al. 2007) relied on deriving average LAE characteristics from stacked LAE samples, but stacked analyses may not reveal the full distribution of LAE characteristics. Most efforts to date have found LAEs to be largely young or of intermediate ages and having characteristically small masses (Gawiser et al. 2007; Pirzkal et al. 2007; Finkelstein et al. 2009; Cowie, Barger & Hu 2011), but SED fitting procedures tend to vary from author to author, making direct comparisons of derived characteristics difficult from sample to sample. In addition, SED fitting procedures for starbursting galaxies have been evolving recently to account for contamination of observed photometry from nebular emission lines. Schaerer & de Barros (2009) and others have demonstrated that failure to include these lines, produced from hot gas in star-forming regions, can drastically alter the ages and masses derived from SED fitting.

In this paper, we present a simple way to account for nebular emission during SED fitting in our sample of 33 spectroscopically confirmed $z \sim 3.1$ LAEs. The technique we outline in this paper allows us to predict the strength of the [O III] nebular emission line, which we can compare to the near-infrared (NIR) detections and upper limits we have made of this line in six $z \sim 3.1$ LAEs.

⋆ E-mail: mclinden@astro.as.utexas.edu

Published by Oxford University Press on behalf of the Royal Astronomical Society

In Section 2, we present the extensive observations that form the foundation of this paper, including an NB survey to find LAE candidates, optical spectroscopy to confirm LAE candidates and NIR spectroscopy to look for rest-frame optical nebular emission lines in these LAEs. We also present our data reduction techniques in this section. In Section 3, we present our results from optical and NIR spectroscopy, including a new [O III] measurement in one LAE and the subsequent velocity offset between [O III] and Lyα that we measure in this object. Section 4 outlines our methods for SED fitting, including the introduction of a new method to account for nebular emission lines in the SED fitting process. We present our results from SED fitting in Section 5. Finally, in Section 6, we discuss the ability of our SED fitting process to match our observations of the [O III] line in LAEs. We also compare our SED results to those presented by other authors.

Where relevant, we adopt the standard cosmological parameters $H_0 = 70$ km s^{-1} Mpc^{-1}, $\Omega_{\rm m} = 0.3$, and $\Omega_\Lambda = 0.7$ (Spergel et al. 2007). Also we use the following vacuum wavelengths, 1215.67 Å for Lyα, 3727.092/3729.875 Å for [O II], 4862.683 Å for Hβ and 4960.295/5008.240 for [O III] from the Atomic Line List v2.04.[1] All quoted magnitudes are AB magnitudes.

2 OBSERVATION AND DATA

2.1 NB survey

We collected data for our NB survey in 2007 (PI: Finkelstein) and 2009 (PI: McLinden) using the 90-inch Bok telescope with the 90 Prime Camera (Williams et al. 2004) at Steward Observatory. The survey was completed in the Cosmological Evolution Survey (COSMOS) field centred at RA 10:00:28.6 and Dec. +02:12:21.0 (J2000) (Capak et al. 2007). The NB data were collected on UT 2007 February 21 and 22. The rest of the NB data, described below, were collected on UT 2009 February 27, 28 and 2009 March 1. We used the KPNO [O III] filter, centred at 5025 Å, with a narrow bandpass of 55Å, to select Lyα emission from z = 3.11 to 3.16. The 90 Prime instrument was originally outfitted with a 1 deg^2 field of view from four 4096 pixel × 4096 pixel CCDs. This was the instrument setup for our 2007 observations. Due to instrument failure however, our 2009 observations were made with only a single 4064 pixel × 4064 pixel CCD, providing less coverage and therefore less depth than we had initially anticipated. The pixel scale for 90 Prime is 0.45 arcsec pixel^{-1}.

To reduce the NB data we used the MSCRED package in IRAF. The data reduction process included bias subtraction, overscan subtraction, flat-fielding and cross-talk correction using CCDPROC. We applied astrometry corrections using the USNO B1.0 catalogue (Monet et al. 2003) with the IRAF tasks MSCTPEAK and MSCCMATCH. Cosmic ray rejection proceeded using the JMCCREJ algorithm developed by Rhoads et al. (2000). Complete bad pixel masks, including manually added satellite trails, were created and applied to each frame before stacking. MSCIMAGE was used to resample individual exposures on to a common pixel grid. Scaling was determined using MSCIMATCH. Before stacking the images, we applied skyflats in CCDPROC and did a sky subtraction using MSCSKYSUB. Finally, we used MSCSTACK to stack each individual frame into a single final exposure. A total of 50 frames, representing 16.67 h of integration, were stacked to create this final 1.96 deg^2 image. We find a 5σ depth of 23.2 mag in a 3 arcsec diameter aperture, which corresponds to a line flux lower limit of ~1.2×10^{-16} erg cm^{-2} s^{-1} for pure emission line sources. The point spread function FWHM (full width at half-maximum) in our final stack is ~3.62 pixels, corresponding to 1.63 arcsec.

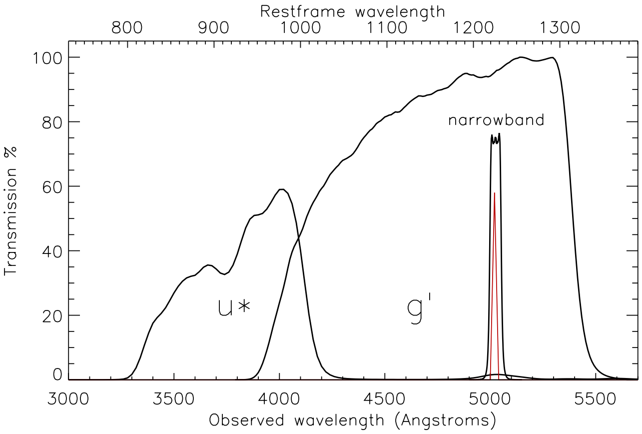

Figure 1. Transmission curves for the u^*, g', and NB filters. The CFHT u^* filter is centred at 3798 Å (dλ = 720 Å), the Subaru g' filter is centred at 4780 Å (dλ = 1265 Å), and the KPNO [O III] narrow-band filter (λ = 5025 Å, dλ = 55 Å) used for our NB survey lies within the g' filter. Also shown is a mock Lyα line (not to scale) in red, inside the NB filter.

2.2 Broadband data for candidate selection

Our NB survey is complemented by a plethora of publicly available data in the COSMOS field. In particular, we used u^*- and g'-band images (McCracken et al. 2010) from the NASA/IPAC archive[2] in concert with our NB survey to select LAEs as described in Section 2.3 below. The u^*-band images come from the MegaPrime instrument (Boulade et al. 2003) on the 3.6 m Canada–France–Hawaii Telescope. The u^* images have a 5σ depth in a 3 arcsec aperture of 26.4 (Capak et al. 2007). The u^* filter is centred at 3798 Å and has a bandpass of 720 Å. The g' images come from Suprime-Cam on the 8.3 m Subaru telescope. The 5σ depth in a 3 arcsec aperture for the g' images is 27.0 (Capak et al. 2007). The g' filter is centred at 4780 Å and has a bandpass of 1265 Å. The filter transmission curves for the u^*, g', and NB are shown in Fig. 1. Note that one of the wide broad-band filters, the g' filter, encompasses the [O III] narrow-band and the other broad-band filter, the u^* band, is fully bluewards of the NB filter and Lyα line. This filter setup is essential for our selection of LAEs via NB imaging because an LAE at $3.11 \geq z \geq 3.16$ ought to have an excess of flux in the NB when compared to the g' band, due to the location of the Lyα line. The LAE SED should also be attenuated bluewards of the Lyα line due to Lyα forest absorption. Our use of the u^* and g' filters with our NB data allows us to detect both this flux excess and attenuation as detailed in Section 2.3 below.

2.3 LAE candidate selection via Source Extractor

We selected LAE candidates based on a combination of their narrow-band and broad-band photometry. To do this, we used Source Extractor (SEXTRACTOR; Bertin & Arnouts 1996) to detect objects and extract their photometry. We used aperture photometry

---

[1] http://www.pa.uky.edu/~peter/atomic/index.html

[2] http://irsa.ipac.caltech.edu/data/COSMOS/datasets.html

measurements (FLUX_APER) from SExtractor, in a 3 arcsec diameter aperture. Objects were extracted from the central 1.44 deg^2 of our NB survey, avoiding some of the shallower edges of our survey.

We extracted fluxes for all objects detected in the NB image by running SExtractor in dual-image mode. In dual-image mode, our NB image was the 'detection' image and a second image, either the NB, u^* or g' image, was 'the measurement' image. The detection image determines where objects are found, the measurement image is used to measure fluxes at those locations. In order to run SExtractor in dual-image mode, both images must have the same pixel scale. To make this possible, we registered the u^* and g' images to the NB image with the iraf tasks WCSMAP and GEOTRAN, where WCSMAP computes a spatial transformation function from the WCS information of the images and GEOTRAN performs this geometric transformation. This process changes the resolution of broad-band images from their native resolution of 0.15 arcsec pixel^{-1} to the 0.45 arcsec pixel^{-1} resolution of the NB image. Such a transformation means measurements can be made in the exact same pixels from image to image. The NASA/IPAC COSMOS archive also includes maps of image rms for all of our broadbands, so we used these as WEIGHT_IMAGES in SExtractor with the SExtractor parameter WEIGHT_TYPE set to MAP_RMS. We created rms maps for our NB image using the CHECK_IMAGE feature of SExtractor.

The final set of confirmed LAEs presented in this paper is a compilation of objects from multiple LAE selections. Our earliest selection of LAEs was performed on an a preliminary reduction of our NB data that only included the 2007 data. Later selections were performed on reductions of the NB data that contained the full 16.67 h of data. Our selection criteria have also evolved since the preliminary selection, as we have honed in on criteria more likely to yield confirmations in optical spectroscopy given our specific combination of very deep broad-band images (u^*, g') and our shallower NB image. In addition, we re-reduced the NB data to try to improve the quality of the final product. This improvement was achieved with additional flat-fielding and chip-by-chip sky subtraction, as well as improved image weighting, and image scaling. Our basic LAE selection criteria are as follows:

$$\frac{f_{\rm NB}}{\delta f_{\rm NB}} \geq 5 \text{ and } \frac{f_g}{\delta f_g} \geq 2 \tag{1}$$

$$\frac{f_{\rm NB}}{f_g} \geq 2 \tag{2}$$

$$\frac{f_{\rm NB} - f_g}{\sqrt{\delta f_{\rm NB}^2 + \delta f_g^2}} \geq 4 \tag{3}$$

$$f_u \leq 10^{-4/5} f_g + 2\delta f_u, \tag{4}$$

where f_u is flux in the u^* band, f_g is flux in the g' band, $f_{\rm NB}$ is flux in the NB band, δf_u is flux error in the u^* band, δf_g is flux error in the g' band, and $\delta f_{\rm NB}$ is flux error in the NB. In other words, to be an LAE candidate, an object must (1) be detected at the 5σ level in the NB and at the 2σ level in the g band, (2) have an excess of flux density in the NB compared to the g band (corresponding to rest-frame equivalent width ≥14.7 Å), (3) that flux excess must be significant at the 4σ level, and (4) the flux bluewards of the Lyα line must be attenuated in a manner congruent with expected Lyα forest absorption. For $z \sim 3.1$, this means that the u^* band should be at least 2 mag fainter than the g' band (Madau 1995), but can amount to somewhat less than 2 mag when you incorporate the u^* error bars. These criteria are based on those developed by Rhoads & Malhotra (2001). We note that the requirement of a detection in the g' band is not a requirement that there be continuum detection, as the presence of the Lyα line can be sufficient to cause a detection in the g' band. 12 of the objects in sample presented in this paper were initially selected with these criteria (labelled as selection 1 in Table 1). Three additional (unique) objects in the sample were selected with a less stringent fourth criterion, i.e. $f_u \leq 10^{-4/5} f_g + 3\delta f_u$ (selection 2). 14 more (unique) LAEs in the sample were selected with an also less stringent fourth criterion, $m_u - m_g > 0.5$ (selection 3). Because the u^*-band data are so much deeper than our NB data we found these less stringent requirements on the suppression of the u-band flux to be useful.

In addition to the traditional NB selection criteria detailed above, we also experimented with finding LAEs using a broad-band detection as the initial requirement. This was possible again because the publicly available broad-band data were so much deeper than our NB survey. Three of the objects in our current sample were selected this way (selection 4). The criteria in this case are as follows:

$$\frac{f_g}{\delta f_g} \geq 5 \tag{5}$$

$$\frac{f_{\rm NB}}{f_g} \geq 1.445 \tag{6}$$

$$\frac{f_{\rm NB} - f_g}{\sqrt{\delta f_{\rm NB}^2 + \delta f_g^2}} \geq 2 \tag{7}$$

$$\frac{f_u}{f_g} < 10^{-2/5}. \tag{8}$$

In other words, the first requirement is a g' detection, not an NB detection as is the case for our NB detection criteria. In addition, the g' detection is required at a higher significance (5σ) than the g' requirements in the NB criteria above. Because we are requiring a g' detection as the preliminary criterion for these objects, we re-ran SExtractor, still in dual-image mode, but now with the g' image as the 'detection' image, and either the g', u^*, or NB image as the 'measurement' image. A strong emission line object in the NB should be well detected in the g' that encompasses the NB. The second criterion still requires that an excess of flux be present in the NB compared to the g band, but the minimum magnitude of this excess is lowered, and the significance of the excess is also lowered (from 4σ to 2σ). Essentially, this only requires a rest-frame equivalent width of ≥6.4 Å. Finally, the u^* flux must still be less than the g' flux, but the difference need not be as large, given the depth of the u^* band.

While the sample of LAEs discussed in this paper comes from a compilation of objects selected from multiple data reductions and different selection iterations, we emphasize that each LAE discussed here has been confirmed spectroscopically (as discussed in Section 2.4). The compilation of multiple extractions is simply a result of the long-term nature of this project and an interest in improving our selection process and results. We can state, a posteriori, a broad set of selection criteria that each object in our sample is subject to, by comparing the four selections and combining the least stringent set of criteria from across the four selections. This leaves us with the four criteria shown below, which all 33 of our confirmed LAEs satisfy:

$$\frac{f_g}{\delta f_g} \geq 2 \tag{9}$$

Table 1. SExtractor photometry of confirmed LAEs and NIR follow-up details.

Object	Flux$_{\mathrm{NB}}$	Flux$_g$ (μJy)	Flux$_u$	EW^a (Å)	Selection	LUCIFER^b (s)	NIRSPEC^c (s)
LAE_J100049.56+021647.1	1.41 ± 0.28	0.62 ± 0.052	0.16 ± 0.028	19. ± 7.0	4		
LAE_J095859.33+014522.0	0.71 ± 0.15	0.37 ± 0.049	0.13 ± 0.047	14. ± 7.0	4		
LAE_J100212.99+020137.7	1.58 ± 0.23	0.29 ± 0.050	0.14 ± 0.037	78. ± 23.0	3		
LAE_J095929.41+020323.5 (LAE6559)	1.53 ± 0.23	0.21 ± 0.043	0.07 ± 0.043	121. ± 43.0	1,2,3	1680^d	1800^d
LAE_J095944.02+015618.8	1.27 ± 0.20	0.21 ± 0.053	0.03 ± 0.067	89. ± 35.0	3		
LAE_J095930.52+015611.0 (LAE7745)	3.42 ± 0.20	0.50 ± 0.047	0.12 ± 0.045	111. ± 17.0	1,3	1680	
LAE_J100217.05+015531.7	1.35 ± 0.22	0.40 ± 0.062	0.21 ± 0.039	37. ± 11.0	3		
LAE_J100157.87+021450.0	1.34 ± 0.23	0.18 ± 0.059	0.02 ± 0.079	131. ± 70.0	3		
LAE_J100124.36+021920.8 (LAE40844)	6.78 ± 0.37	1.25 ± 0.073	0.22 ± 0.074	78. ± 8.0	1,2	1200	
LAE_J095847.81+021218.2	1.73 ± 0.26	0.40 ± 0.019	0.09 ± 0.054	55. ± 11.0	1		
LAE_J095904.93+015355.4	0.99 ± 0.14	0.14 ± 0.011	0.03 ± 0.069	121. ± 26.0	1		
LAE_J095910.90+020631.6 (LAE14310)	3.45 ± 0.38	0.58 ± 0.073	0.24 ± 0.072	89. ± 20.0	1,2	6000^d	
LAE_J095921.06+022143.4	1.13 ± 0.16	0.25 ± 0.015	0.07 ± 0.052	57. ± 11.0	1		
LAE_J095948.47+022420.8	1.11 ± 0.15	0.16 ± 0.011	0.00 ± 0.001	114. ± 22.0	1,2		
LAE_J100019.07+022523.9 (LAE27878)	1.68 ± 0.25	0.24 ± 0.046	0.09 ± 0.051	118. ± 40.0	1,2	4800	
LAE_J100100.35+022834.7	2.48 ± 0.25	0.46 ± 0.014	0.09 ± 0.066	76. ± 10.0	1		
LAE_J100146.04+022949.0	0.90 ± 0.14	0.16 ± 0.011	0.07 ± 0.041	79. ± 17.0	1		
LAE_J095843.11+020312.3	1.70 ± 0.22	0.36 ± 0.014	0.13 ± 0.039	63. ± 11.0	1		
LAE_J100128.11+015804.7	1.36 ± 0.21	0.31 ± 0.040	0.02 ± 0.125	58. ± 15.0	2		
LAE_J100017.84+022506.1 (LAE27910)	1.57 ± 0.22	0.30 ± 0.042	0.09 ± 0.045	73. ± 19.0	2	1800^d	
LAE_J095839.92+023531.3	1.53 ± 0.25	0.43 ± 0.017	0.16 ± 0.053	40. ± 9.0	1		
LAE_J095838.90+015858.2	1.08 ± 0.18	0.08 ± 0.009	0.03 ± 0.048	452. ± 198.0	1,2		
LAE_J100020.70+022927.0	1.13 ± 0.22	0.18 ± 0.041	0.14 ± 0.040	98. ± 39.0	2		
LAE_J095812.33+014737.6	1.10 ± 0.18	0.59 ± 0.048	0.22 ± 0.057	13. ± 5.0	4		
LAE_J095920.42+013917.1	1.10 ± 0.16	0.58 ± 0.054	0.20 ± 0.056	13. ± 4.0	4		
LAE_J095846.72+013706.1	1.18 ± 0.18	0.24 ± 0.072	0.04 ± 0.106	66. ± 29.0	3		
LAE_J095923.79+013045.6	1.37 ± 0.20	0.16 ± 0.061	0.02 ± 0.133	154. ± 94.0	3		
LAE_J100213.17+013226.8	1.19 ± 0.23	0.18 ± 0.062	0.04 ± 0.087	105. ± 57.0	3		
LAE_J095838.94+014107.9	1.03 ± 0.17	0.21 ± 0.045	0.07 ± 0.075	69. ± 25.0	3		
LAE_J095834.43+013845.6	2.01 ± 0.19	0.22 ± 0.046	0.09 ± 0.063	182. ± 67.0	3		
LAE_J100302.10+022406.7	3.87 ± 0.39	0.39 ± 0.046	0.20 ± 0.052	206. ± 50.0	3		
LAE_J100157.45+013556.2	2.09 ± 0.19	0.39 ± 0.078	0.17 ± 0.068	75. ± 22.0	3		
LAE_J100152.14+013533.2	1.36 ± 0.19	0.41 ± 0.077	0.14 ± 0.068	36. ± 11.0	3		

[a] Rest-frame.
[b] Exposure time using LUCIFER on LBT.
[c] Exposure time using NIRSPEC on Keck.
[d] Non-detection.

$$\frac{f_{\mathrm{NB}}}{f_g} \geq 1.445 \tag{10}$$

$$\frac{f_{\mathrm{NB}} - f_g}{\sqrt{\delta f_{\mathrm{NB}}^2 + \delta f_g^2}} \geq 2 \tag{11}$$

$$\frac{f_u}{f_g} < 10^{-2/10}. \tag{12}$$

2.4 Optical spectroscopy

We obtained optical spectroscopy of our LAE candidates using the Hectospec multifibre spectrograph (Fabricant et al. 2005) at the 6.5 m MMT Observatory (a joint facility of the Smithsonian Astrophysical Observatory and the University of Arizona) in 2009 and 2011. Hectospec has 300 optical fibres, a 1 deg^2 field of view, and spectral coverage from 3650 to 9200 Å. We used the 270 lines per mm grating for our observations. This setup has a blaze wavelength of ∼5200 Å and dispersion of 1.21 Å pixel^{-1}. The resolution of the instrument is ∼6 Å. Optical spectroscopy allows us to the confirm the presence of the Lyα line in the candidate's spectrum, thereby assuring us the object is indeed an LAE at $z \sim 3.1$. We rule out [O II] emitters at $z \sim 0.34$ and [O III] emitters at $z \sim 0$ by looking for other optical lines that would be present in such cases. Also, the presence of high-ionization lines in addition to the Lyα line, such as C IV redshifted to $\lambda \sim 6350$ Å, also help us distinguish between star-forming galaxies at $z \sim 3$ and objects that are likely AGN. Our initial Hectospec data were obtained on UT 2009 February 16 and 21 and April 26 and 27 (PI: Malhotra). Our reductions for the 2009 data combine 120 min of observations per object. Our newest LAE candidates were observed on UT 2011 March 25 and 26 (PI: McLinden). Our reductions for the 2011 data combine either 150 or 330 min of observations for each object.

2.4.1 *Reduction of optical spectra*

We reduced the optical spectra of our LAE candidates observed in 2011 using HSRED, an IDL-based reduction package.[3] HSRED is mostly based on SPECROAD, SAO's Hectospec reduction package. The reduction process bias corrects and flat-fields the fibres and removes

---

[3] http://astro.princton.edu/ rcool/hsred.

cosmic rays. Traces of the 300 fibres are made from the domeflats and a wavelength solution is derived from a HeNeAr arc lamp exposure using a fifth-order Legendre polynomial. Accurate sky models are determined from dedicated sky fibres included in each observation. Sky-subtracted 1D spectra are extracted. The average residual from the wavelength calibration is ∼0.2 Å. Median-combined spectra are created by combining multiple observations that have the same instrument/fibre setup. See Papovich et al. (2006) for more detail on each of these steps.

We chose to flux calibrate our optical spectra outside the reduction pipeline. We scaled a G8III spectral-type Pickles model (Pickles 1998) spectrum to match the $V \sim 5.36$ magnitude of our observed G8III spectral-type standard star. Before scaling, the Pickles model has zero magnitude in Vega magnitudes. We divided the scaled-down Pickles spectrum by the standard star's spectrum in counts to create a sensitivity curve. We then multiplied each reduced, uncalibrated optical spectrum (in counts) by this sensitivity curve to get a flux-calibrated spectrum in erg $\mathrm{s^{-1}\,cm^{-2}\,Å^{-1}}$. The 33 LAEs discussed in this paper include 18 objects that were observed, reduced and confirmed in 2011.

The LAEs observed with Hectospec in 2009 were previously reduced with the External SPECROAD[4] pipeline developed by Juan Cabanela, as described previously in McLinden et al. (2011). ESPECROAD applies bias, dark and flat-field corrections and wavelength calibration (using He–Ne–Ar arc lamps).

Our 2009 data were not flux calibrated, but we were able to use LAEs that were observed both in 2011 and 2009 to go back and flux calibrate the 2009 data. Four objects were observed in both years, and we chose to use the two brightest objects, with the highest signal to noise ratios (SNR), to derive a scale factor that would appropriately calibrate the 2009 data. To derive this scale factor, we compared the Lyα line flux in these two bright LAEs, in the flux-calibrated (2011) data and the non-flux-calibrated (2009) data. The line flux in the uncalibrated case is in units of counts Å. The line flux in the calibrated spectra are in units erg $\mathrm{s^{-1}\,cm^{-2}}$. The scale factor is then this calibrated line flux divided by the uncalibrated line flux, yielding a constant with units erg $\mathrm{s^{-1}\,cm^{-2}\,Å^{-1}\,counts^{-1}}$. Therefore, when this constant is multiplied by an uncalibrated spectrum with units counts, the result is an appropriately scaled spectrum with units erg $\mathrm{s^{-1}\,cm^{-2}\,Å^{-1}}$. The constants from the brightest two LAEs, derived as described above, were averaged. The averaged value was then used to flux calibrate the rest of the 2009 data. This procedure was used to flux calibrate a total of 15 LAEs from 2009, among our larger sample of 33 confirmed LAEs. The 1D optical spectra of all 33 confirmed LAEs are shown in Figs 2–4.

2.5 Construction of the final sample

Combining the object selection methods and spectroscopic confirmations discussed above, we have a sample of 33 LAEs. The photometry (from SEXTRACTOR) for these 33 confirmed LAEs is shown in Table 1. This total does not include two Lyα-emitting objects (LAE25972, LAE42795) that were removed because they are likely AGN (see Section 3.3). The AGN are excluded from discussion of our SED fitting results (Section 4) as their physical characteristics cannot be derived from comparison to star-forming SED models. We note that eight of our 33 LAEs have poor agreement between measured spectroscopic and photometric Lyα line fluxes; they are not removed from the sample but are labelled as such later in this paper (Tables 2 and 3). An additional 5 of these 33 LAEs have possible multiple components and/or morphology indicative of possible interacting sources (Malhotra et al. 2012). This was determined by finding objects that had multiple matches within 2 arcsec in the COSMOS ACS Catalog (Leauthaud et al. 2007). We confirmed the multicomponent morphology with visual inspection of the corresponding *Hubble Space Telescope* (*HST*) ACS *F*814*W* images (Koekemoer et al. 2007; Massey et al. 2010). Note that fitting SED models to photometry that may be from multiple sources can certainly affect what characteristics are derived from SED fitting results. These five objects are also labelled in Tables 2 and 3.

2.6 New NIR spectroscopy

We observed 5 $z \sim 3.1$ Lyα-emitting objects from our sample of 33 LAEs in the NIR. These observations are in addition to the three LAEs previously observed in the NIR with LUCIFER, as detailed in McLinden et al. (2011, hereafter Mc11). We made our NIR observations using LUCIFER (LBT NIR Spectrograph Utility with Camera and Integral-Field Unit for Extragalactic Research) on the 8.4 m LBT (Seifert et al. 2003; Ageorges et al. 2010) and using NIRSPEC on the 10 m Keck II telescope (McLean et al. 1998). The previously observed LAEs in Mc11 were LAE40844, LAE27878, and LAE14310. LAE40844 and LAE27878 yielded detections of the [O III] line. Of the five new observations, two yielded [O III] detections, but one of these [O III]-detected objects was among the objects removed as likely an AGN (see Section 3.3). The other new detection, henceforth LAE7745, appears to be a typical star-forming LAE, and will be discussed in more detail below. No emission lines were detected in the other three observed objects, henceforth LAE25972, LAE6559, and LAE27910.

2.7 New LUICFER data

We used the longslit mode of LUCIFER for two of our new NIR observations in the same manner as our previous LUCIFER observations (Mc11) – with a 1 arcsec slit utilizing the H+K grating with 200 lines $\mathrm{mm^{-1}}$ and the N1.8 camera. The image scale of the N1.8 camera is 0.25 arcsec $\mathrm{pixel^{-1}}$. LAE25972 was observed over ten 120 s frames. LAE7745 and LAE6559 were observed over seven 240 s frames. The longslit was oriented such that each LAE shared the longslit with a bright ($R \sim 12$–18) continuum object.

2.7.1 2D reduction of NIR LUCIFER spectra

We reduced the 2D LUCIFER spectra using NIRSPEC_REDUCE, a package of IDL scripts written by Becker et al. (2006). NIRSPEC_REDUCE follows the methodology of Kelson (2003) for optimal sky subtraction. In this technique, the sky subtraction is performed by subsampling the raw (distortion uncorrected) spectra thereby improving the sky subtraction significantly. We customized the scripts to accommodate LUCIFER data. The first three scripts in the reduction process, NIRSPEC_SLITGRID, NIRSPEC_WAVEGRID and NIRSPEC_FLATFIXER were all modified to deal with LUCIFER's 2048 pixel × 2048 pixel array as opposed to NIRSPEC's 1024 pixel × 1024 pixel array. NIRSPEC_SLITGRID transforms x- and y-coordinates to coordinates of slit position, and NIRSPEC_WAVEGRID transforms x- and y-coordinates to coordinates of uncalibrated wavelength. NIRSPEC_FLATFIXER creates a median-combined normalized flat and a separate file containing the variance in the median-combined normalized flat. We used three 5 s Halo2 flats for each reduction.

---

[4] http://iparrizar.mnstate.edu/~juan/research/ESPECROAD/index.php

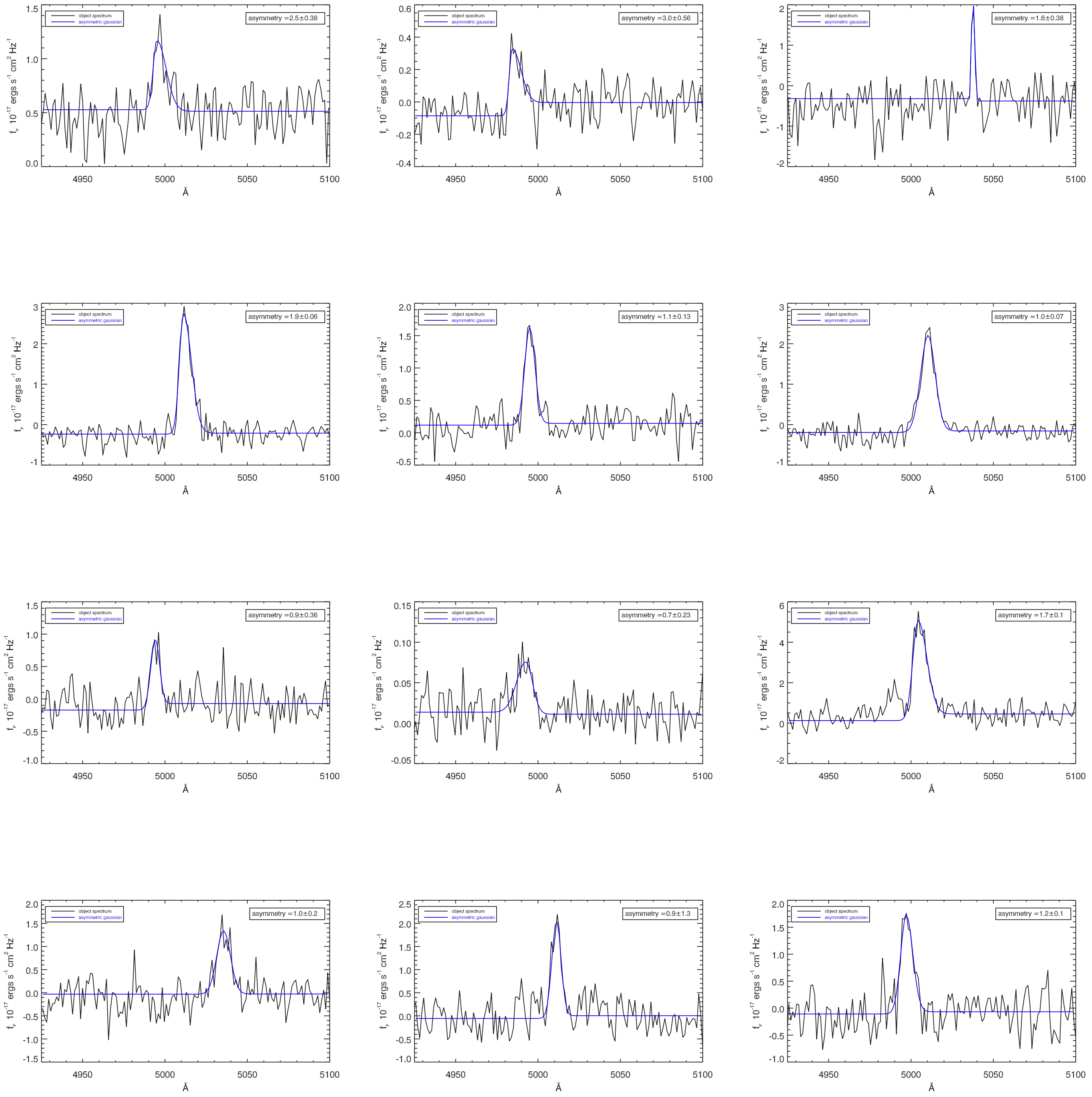

Figure 2. 1D optical spectra of first 12 confirmed LAEs. The order of objects matches the order of objects in Tables 1–3 (reading spectra from top left to bottom right). Asymmetry of Lyα line is shown at top left of each panel, observed spectrum is in black, best-fitting asymmetric Gaussian is overlaid in blue.

The final script in the process, the one that actually performs the sky subtraction, LONGSLIT_REDUCE, was not directly modified. Parameters for a specific instrument can be supplied to this script via an external LONGSLIT_REDUCE.inc file. Therefore, appropriate values for LUCIFER for information, such as array size, gain, slit width, observatory location etc., can be easily supplied without modifying the actual script. As noted in the README file supplied with the NIRSPEC_REDUCE package, to subtract an accurate sky model this program processes a raw frame, locates and masks objects, iteratively fits the sky in a single frame to get sky levels and iteratively fits the sky in a differenced frame and then subtracts the fit. The program can also provide wavelength calibration and extract a 1D spectrum but we only used this package to produce reduced sky-subtracted 2D frames.

Finally, individual frames for each object, output from NIRSPEC_REDUCE, were median combined with IRAF task IMCOMBINE. Nods along the slit were removed by providing integer pixel offsets in the spatial direction using the ‘offsets’ parameter in IMCOMBINE to bring all the frames to the position of the first frame. For LAE25972, ten 120 s frames were median combined. For LAE7745 and LAE6559, the seven 240 s frames were median combined.

Only one object, LAE7745, shows a detection in the reduced 2D (Fig. 5). The detection corresponds to the expected spatial-direction location of the LAE based on its distance from the bright

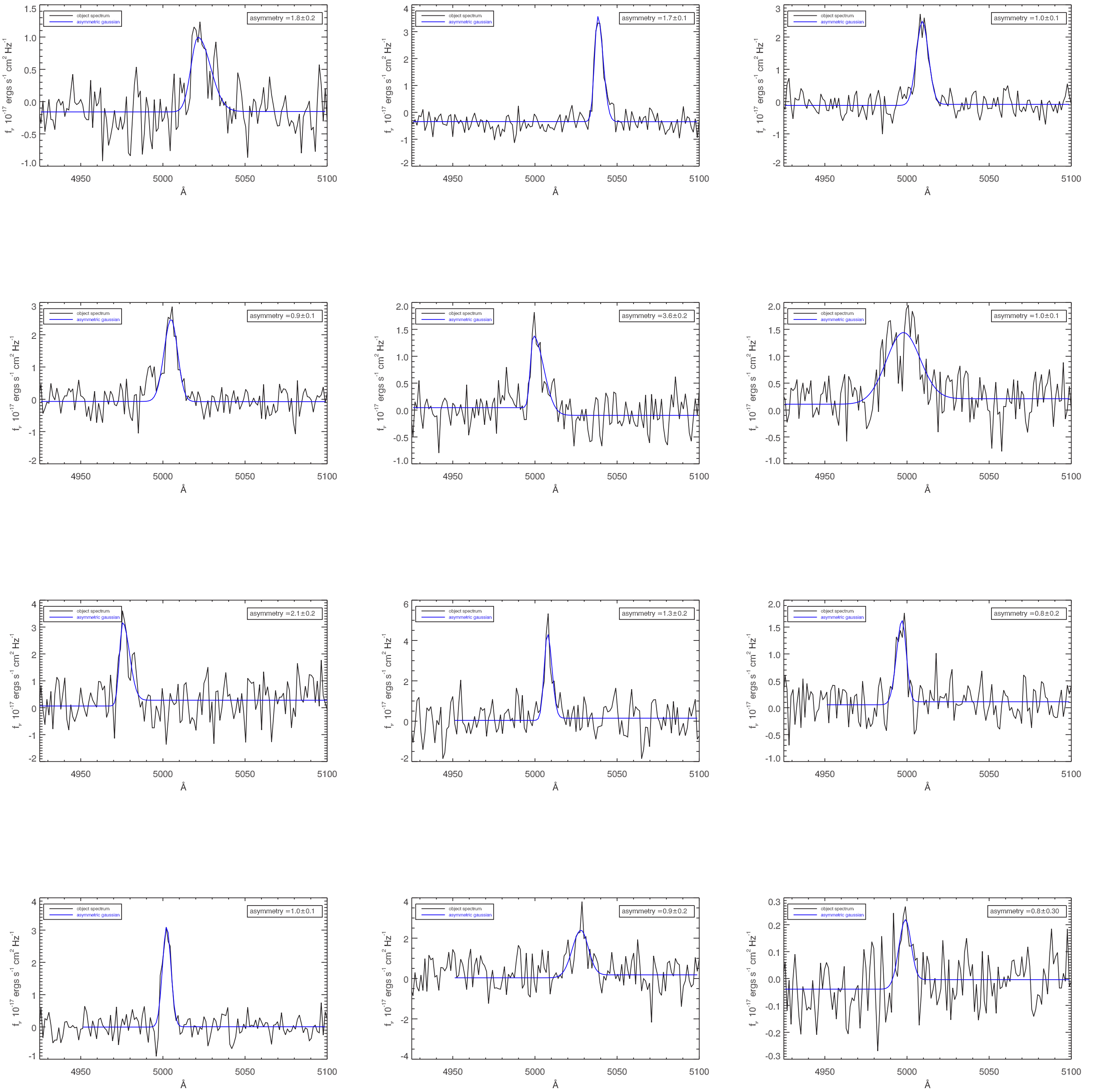

Figure 3. Continuation of Fig. 2 – 1D optical spectra of next 12 confirmed LAEs. The order of objects matches the order of objects in Tables 1–3 (reading spectra from top left to bottom right). Asymmetry of Lyα line is shown at top left of each panel, observed spectrum is in black, best-fitting asymmetric Gaussian is overlaid in blue.

continuum object that shared the slit. The detection also corresponds to the approximate expected dispersion-direction location of an [O III] detection based on the Lyα redshift of $z \sim 3.1$. Given that this detection appears at both the expected spatial and dispersion locations gives strong credibility to this being a real detection of [O III] and not an errant cosmic ray. In addition, while the detection cannot be seen in a single exposure, it can be seen faintly when a single exposure is subtracted from a nodded subsequent exposure. The other two objects show no detections and are shown in the bottom panel of Fig. 5. Possible reasons for non-detections are insufficient integration time for faint lines and emission lines located under OH skylines. We argue in Section 6.1 that insufficient integration time is a likely culprit for these two non-detections.

2.7.2 1D reduction of LUCIFER spectra

The 1D spectra were created following a similar reduction process to that outlined in Mc11. We utilized the DOSLIT routine in IRAF (Valdes 1993). Because a bright continuum source shared the slit with each LAE, we were able to create a trace for extraction from the bright object. The trace was then shifted along the spatial axis to extract the LAE spectrum, whose continuum emission is

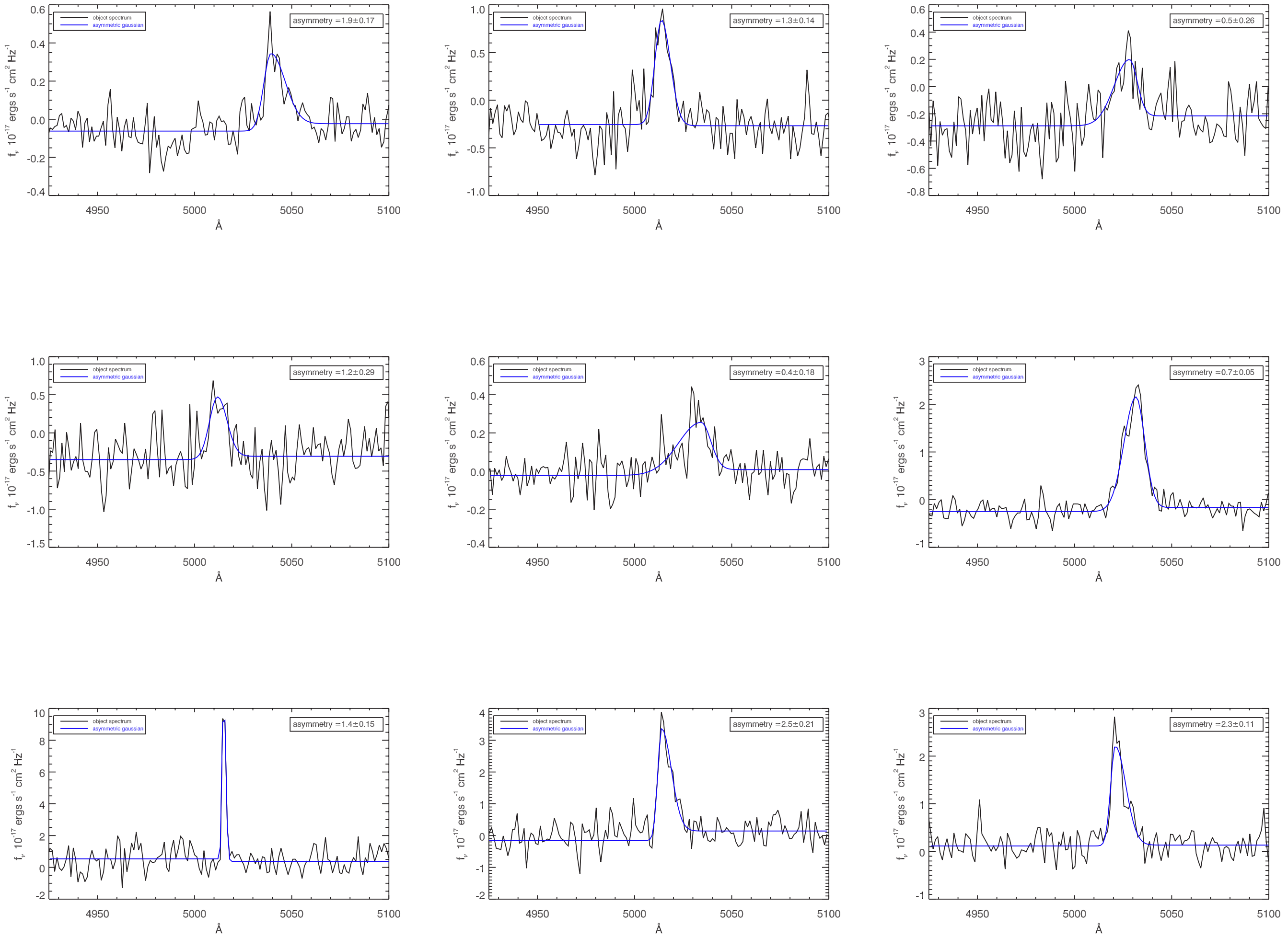

Figure 4. Continuation of Figs 2 and 3 – 1D optical spectra of final nine confirmed LAEs. The order of objects matches the order of objects in Tables 1–3 (reading spectra from top left to bottom right). Asymmetry of Lyα line is shown at top left of each panel, observed spectrum is in black, best-fitting asymmetric Gaussian is overlaid in blue.

undetectably faint in individual exposures and therefore cannot be traced. DOSLIT was performed on the median-combined, sky-subtracted 2D spectra from NIRSPEC_REDUCE. Wavelength calibration was done using night sky OH lines. The average rms uncertainty from wavelength calibration for LAE7745 is ∼0.66 Å. Residual bright night sky lines were interpolated over using the SKYINTERP task from the WMKONSPEC package originally designed for Keck NIRSPEC reduction.[5]

Flux calibration proceeded, as in Mc11, using the bright continuum sources that shared the slit with our LAEs. LAE7745 was calibrated using SDSS J095930.35+015646.6. We flux calibrated the spectrum of the bright continuum star spectrum using an appropriate Pickles model spectrum (Pickles 1998), scaled in flux to match the object's apparent *V* magnitude of the object that shared the slit. We determined the appropriate Pickles model spectrum to use by determining the star's spectral type from SDSS $u-g$ and $g-r$ colours (Fukugita et al. 2011). The SDSS *u*, *g*, and *r* magnitudes for this determination come from SDSS data release seven. The *V* magnitude of the observed calibration star was determined from its SDSS colours and the Lupton colour transformation from SDSS $g-r$ colour to *V* magnitude.[6] The sensitivity curve for calibration comes from dividing the scaled-down Pickles model by the bright continuum star's stellar spectrum in counts. The raw LAE spectrum was multiplied by the sensitivity curve to produce a final flux-calibrated NIR LAE spectrum. This method ought to account for slit losses automatically, provided that slit losses are the same for both the on-slit continuum source and the LAE.

2.8 NIRSPEC data and reduction

Two of our five additional NIR observations were made at the Keck II telescope using NIRSPEC. Observations were made on 2010 January 30 and February 1. We used the 42 × 0.76 arcsec slit and the low-resolution mode of NIRSPEC for these observations. For LAE42795, we obtained nine 360 s frames of the *K*-band spectroscopy, using the blocking filter NIRSPEC-7 and seven 600 s frames of the *H*-band spectroscopy, using the blocking filter NIRSPEC-5. The *K*-band spectra show a very broad [O III] emission line. In Section 3.3, we discuss our interpretation of this broad line as evidence of AGN activity. For LAE27910, we obtained five 360 s frames of the *K*-band spectroscopy using the NIRSPEC-7

---

[5] http://www2.keck.hawaii.edu/inst/nirspec/wmkonspec.html

[6] http://www.sdss.org/dr7/algorithms/sdssUBVRITransform.html

Table 2. Best allowed-fit parameters from SED fitting for each object in our sample, excluding AGN. Mass is in $M_{\odot}$, τ is *e*-folding time for star formation, in Gyr, age_{SFR} is the star-formation-weighted age, in years, Metal is metallicity in $Z_{\odot}$, $E(B-V)$ is standard colour excess from dust attenuation, [O III] is predicted [O III] line flux in erg s^{-1} cm^{-2}, χ_r^2 is reduced chi-square of the best allowed-fit model. 68 per cent confidence ranges (CR) are also given for each parameter. Continued in Table 3.

Object	Mass (log)	68 per cent CR	τ	68 per cent CR	Age[d] (log)	68 per cent CR	Metal	68 per cent CR	$E(B-V)$	68 per cent CR	[O III][c]	68 per cent CR	χ_r^2
LAE_J100049.56+021647.1[b]	9.91	9.88–9.92	1.0e−01	1.0e−01 to 1.0e−01	8.12	8.12–8.12	0.020	0.020–0.020	0.00	0.00–0.05	0.00	0.00–0.00	16.4
LAE_J095859.33+014522.0	9.20	9.14–9.32	1.0e−03	1.0e−04 to 1.0e−03	6.56	6.53–6.71	1.000	1.000–1.000	0.20	0.15–0.20	0.90	0.53–1.18	35.4
LAE_J100212.99+020137.7	8.76	8.75–9.07	1.0e−04	1.0e−04 to 1.0e−03	6.53	6.33–6.59	1.000	1.000–1.000	0.15	0.15–0.20	0.00	0.00–0.00	29.6
LAE_J095929.41+020323.5[a] (LAE6559)	8.38	8.15–8.51	1.0e−04	1.0e−04 to 1.0e−03	6.15	6.21–6.70	1.000	0.005–1.000	0.10	0.05–0.10	0.23	0.00–0.30	6.8
LAE_J095944.02+015618.8	9.73	9.30–9.77	1.0e+00	−1.0e+00 to 4.0e+00	8.66	7.95–8.78	0.005	0.005–0.200	0.00	0.00–0.05	0.00	0.00–0.07	2.4
LAE_J095930.52+015611.0 (LAE7745)	9.41	9.40–9.89	−1.0e−01	−1.0e+00 to 1.0e−01	8.00	7.85–8.78	0.200	0.005–0.400	0.05	0.00–0.05	1.47	1.37–1.59	12.6
LAE_J100217.05+015531.7[b]	10.16	8.95–10.18	1.0e+00	1.0e−04 to 4.0e+00	8.49	6.71–8.54	1.000	1.000–1.000	0.00	0.00–0.10	0.00	0.00–0.43	48.3
LAE_J100157.87+021450.0[a]	8.73	8.38–8.95	1.0e−04	1.0e−04 to 1.0e−03	6.96	6.40–6.98	1.000	0.020–1.000	0.05	0.05–0.15	0.28	0.16–0.52	3.5
LAE_J100124.36+021920.8 (LAE40844)	9.34	9.14–9.34	1.0e−04	1.0e−04 to 1.0e−03	6.83	6.56–6.83	0.200	0.200–0.200	0.10	0.10–0.15	3.71	3.63–4.12	9.1
LAE_J095847.81+021218.2	8.26	8.27–8.65	1.0e−04	1.0e−04 to 1.0e−02	6.59	6.48–6.86	1.000	1.000–1.000	0.00	0.00–0.05	0.75	0.57–0.86	2.7
LAE_J095904.93+015355.4[a]	8.24	8.03–8.54	1.0e−03	1.0e−04 to 1.0e−03	6.70	6.40–6.71	0.005	0.005–0.005	0.10	0.05–0.15	0.00	0.00–0.00	4.1
LAE_J095910.90+020631.6[b] (LAE14310)	8.44	8.18–9.19	1.0e−02	−1.0e−01 to 1.0e−01	6.86	6.56–8.00	1.000	0.200–1.000	0.05	0.05–0.05	0.21	0.00–0.33	7.3
LAE_J095921.06+022143.4	9.91	8.92–9.92	1.0e−02	1.0e−04 to 1.0e−02	7.58	6.65–7.58	0.005	0.005–1.000	0.20	0.15–0.20	0.27	0.13–0.51	2.2
LAE_J095948.47+022420.8[a]	8.16	8.07–8.29	1.0e−04	1.0e−04 to 1.0e−03	6.65	6.59–6.65	0.005	0.005–0.005	0.10	0.10–0.15	0.57	0.44–0.69	7.2
LAE_J100019.07+022523.9 (LAE27878)	8.68	8.42–9.37	1.0e−02	−1.0e−01 to 1.0e−02	6.39	6.42–8.00	0.005	0.005–0.020	0.15	0.10–0.15	0.07	0.00–0.26	2.4
LAE_J100100.35+022834.7	8.84	8.59–8.86	−1.0e−01	−1.0e−01 to 1.0e−02	6.47	6.46–6.70	0.005	0.005–0.005	0.15	0.10–0.15	1.21	1.05–1.29	7.0
LAE_J100146.04+022949.0	10.78	10.69–10.78	1.0e−01	1.0e−01 to 1.0e−01	8.49	8.49–8.49	1.000	0.400–1.000	0.10	0.10–0.10	0.52	0.51–1.00	6.7
LAE_J095843.11+020312.3[b]	8.32	8.30–8.36	1.0e−04	1.0e−04 to 1.0e−03	6.59	6.56–6.59	0.200	0.200–0.200	0.05	0.05–0.05	0.00	0.00–0.00	18.1
LAE_J100128.11+015804.7[a]	8.91	8.71–9.08	1.0e−02	−1.0e−01 to 1.0e−02	6.79	6.53–7.07	0.400	0.005–1.000	0.15	0.10–0.20	1.27	1.16–1.37	24.0
LAE_J100017.84+022506.1 (LAE27910)	8.48	8.24–8.51	1.0e−02	1.0e−04 to 1.0e−02	6.46	6.46–6.65	0.005	0.005–0.005	0.10	0.05–0.10	0.60	0.30–0.72	2.2
LAE_J095839.92+023531.3	9.01	8.74–9.08	1.0e−04	1.0e−04 to 1.0e−04	6.34	5.42–6.40	0.005	0.005–1.000	0.20	0.15–0.20	0.00	0.00–0.14	35.2
LAE_J095838.90+015858.2[a]	7.85	7.84–8.09	1.0e−03	1.0e−04 to 1.0e−03	6.56	6.53–6.59	0.005	0.005–0.005	0.10	0.10–0.15	0.30	0.11–0.37	7.9
LAE_J100020.70+022927.0[a, b]	8.08	8.02–8.13	1.0e−04	1.0e−04 to 1.0e−03	6.59	6.49–6.59	0.005	0.005–0.005	0.05	0.05–0.05	0.18	0.06–0.45	10.9
LAE_J095812.33+014737.6[a]	10.35	9.39–10.07	1.0e−01	1.0e−04 to 1.0e−02	7.95	6.56–7.66	0.005	0.200–0.200	0.15	0.15–0.20	1.19	0.86–1.52	5.2
LAE_J095920.42+013917.1	8.85	8.83–8.94	1.0e−04	1.0e−04 to 1.0e−04	6.71	6.65–6.77	1.000	1.000–1.000	0.05	0.05–0.10	1.20	0.87–1.47	4.6
LAE_J095846.72+013706.1	8.44	8.26–8.73	1.0e−04	1.0e−04 to 1.0e−04	6.47	6.34–6.56	1.000	1.000–1.000	0.10	0.05–0.15	0.32	0.00–0.55	4.6

[a] Poor agreement between spectroscopic and photometric Lyα line flux measurements.
[b] Possible multiple components in *HST* ACS image.
[c] Predicted [O III] line flux, units are 10^{-16} erg s^{-1} cm^{-2}.
[d] Age is age_{SFR}, i.e. star-formation weighted age.

Table 3. Continued from Table 2. Best allowed-fit parameters from SED fitting for each object in our sample, excluding AGN. Mass is in $M_{\odot}$, τ is e-folding time for star formation, in Gyr, age_{SFR} is the star formation weighted age, in years, Metal is metallicity in $Z_{\odot}$, $E(B-V)$ is standard colour excess from dust attenuation, [O III] is predicted [O III] line flux in $erg\,s^{-1}\,cm^{-2}$, χ_r^2 is reduced chi-square of the best allowed-fit model. 68 per cent confidence ranges (CR) are also given for each parameter.

Object	Mass (log)	68 per cent CR	τ	68 per cent CR	Age[d] (log)	68 per cent CR	Metal	68 per cent CR	$E(B-V)$	68 per cent CR	[O III][c]	68 per cent CR	χ_r^2
LAE_J095923.79+013045.6	10.55	10.55–11.37	1.0e−04	1.0e−04 to 1.0e−03	6.65	6.40–7.58	1.000	0.005–1.000	0.70	0.65–0.85	3.43	3.23–4.43	4.1
LAE_J100213.17+013226.8	8.04	8.00–9.92	1.0e−04	1.0e−04 to 1.0e+00	6.59	6.53–8.83	1.000	0.020–1.000	0.05	0.00–0.10	0.12	0.00–0.23	30.4
LAE_J095838.94+014107.9	8.18	8.01–9.50	1.0e−04	1.0e−04 to 1.0e−04	6.59	6.59–8.54	0.005	0.005–0.005	0.05	0.00–0.05	0.88	0.69–1.02	0.9
LAE_J095834.43+013845.6	8.29	8.28–8.58	1.0e−04	1.0e−04 to 1.0e−04	6.53	6.53–6.65	0.005	0.005–0.005	0.10	0.10–0.15	1.16	0.87–1.23	5.2
LAE_J100302.10+022406.7	9.29	9.29–9.50	1.0e−04	1.0e−04 to 1.0e−04	6.53	6.47–6.53	1.000	1.000–1.000	0.20	0.20–0.25	0.00	0.00–0.28	10.0
LAE_J100157.45+013556.2	9.14	8.62–9.45	−1.0e−01	−1.0e−01 to 1.0e−02	7.50	6.53–8.00	1.000	0.020–1.000	0.05	0.05–0.15	1.25	0.69–1.44	3.9
LAE_J100152.14+013533.2	9.85	8.45–9.88	−1.0e+00	−1.0e+00 to 1.0e+00	8.54	6.53–8.54	0.400	0.005–0.400	0.00	0.00–0.05	2.10	1.90–2.28	15.8

[a] Poor agreement between spectroscopic and photometric Lyα line flux measurements.
[b] Possible multiple components in *HST* ACS image.
[c] Predicted [O III] line flux, units are $10^{-16}\,erg\,s^{-1}\,cm^{-2}$.
[d] Age is age_{SFR}, i.e. star-formation weighted age.

filter. We saw no evidence of [O III] or any other optical emission lines in LAE27910. In addition, LAE6559 was observed with NIRSPEC in addition to LUCIFER, but yielded no detections with either instrument. The Keck observations for LAE6559 consisted of five 360 s frames of the *K*-band spectroscopy using the NIRSPEC-7 filter.

We reduced the NIRSPEC data again using the NIRSPEC reduction package (Becker et al. 2006). For this reduction, the spectra were first flat-fielded, and then corrected for dark current using a constant value. The sky was then subtracted again using the optimal sky-subtraction technique of Kelson (2003).

In order to correct for the distortion in both the *x*- and *y*-directions, we use the IRAF tasks XDISTCOR and YDISTCOR in the WMKONSPEC package specifically developed for the NIRSPEC data reduction. All pixels affected by cosmic rays are identified using the IRAF task CRMEDIAN, and these affected pixels are replaced by average counts calculated from neighbouring pixels. We then average-combined each individual spectra using IRAF task IMCOMBINE, for each of the sources. We detected no optical emission lines in any object except the likely AGN (LAE42795).

3 RESULTS FROM OPTICAL AND NIR SPECTROSCOPY

3.1 Lyα line fluxes and asymmetries

We are able to measure Lyα line fluxes in our sample by fitting an asymmetric Gaussian to each line detected in our optical spectroscopy data. A more detailed description of this process is found in Mc11. To summarize, each Lyα line is fitted with an asymmetric Gaussian using a modified version of the ARM_ASYMGAUSSFIT IDL routine developed by Andrew Marble.[7] The purpose of using a fitting routine that allows for, but does not require, an asymmetric solution is that it allows the red and blue sides of the Lyα line to be fitted with different sigmas. In cases where the red-wing of the Lyα is elongated and/or the blue side of the line is sharply truncated, this asymmetric fitting procedure will find a good fit that captures these characteristics. Asymmetric line profiles are observed for high-z LAEs (Rhoads et al. 2003; Dawson et al. 2004; Kashikawa et al. 2006) because the blue side of the line will be preferentially absorbed by intervening neutral hydrogen. In addition, it has been shown that asymmetric Lyα lines can also be produced by Lyα radiative transfer through expanding shells, a model meant to represent outflows from starbursting galaxies (e.g. Verhamme, Schaerer & Maselli 2006; Verhamme et al. 2008). The Lyα line flux is determined from the area under the asymmetric Gaussian. The average Lyα line flux of our entire confirmed sample is $17.4 \pm 0.9 \times 10^{-17}\,erg\,s^{-1}\,cm^{-2}$. We quantify the asymmetry of the fitted Lyα lines as a_{rb}, which comes directly from our asymmetric fitting process, where a_{rb} is the ratio of the red-side best-fitting sigma to the blue-side best-fitting sigma, or $a_{rb} = \sigma_{red}/\sigma_{blue}$. From this definition, when a_{rb} is >1.0, the line is considered asymmetric in the expected direction for Lyα, i.e. with a larger red-side sigma. When a_{rb} is < 1.0, the line is also asymmetric but with a larger blue-side sigma, and when $a_{rb} = 1$, the line is symmetric. The average asymmetry, using this measure, of our entire confirmed sample of LAEs is 1.4 ± 0.2, indicating that, as a whole, our sample of LAEs does have asymmetric Lyα lines. A histogram of Lyα line asymmetries is shown in Fig. 6.

---

[7] http://hubble.as.arizona.edu/idl/arm/

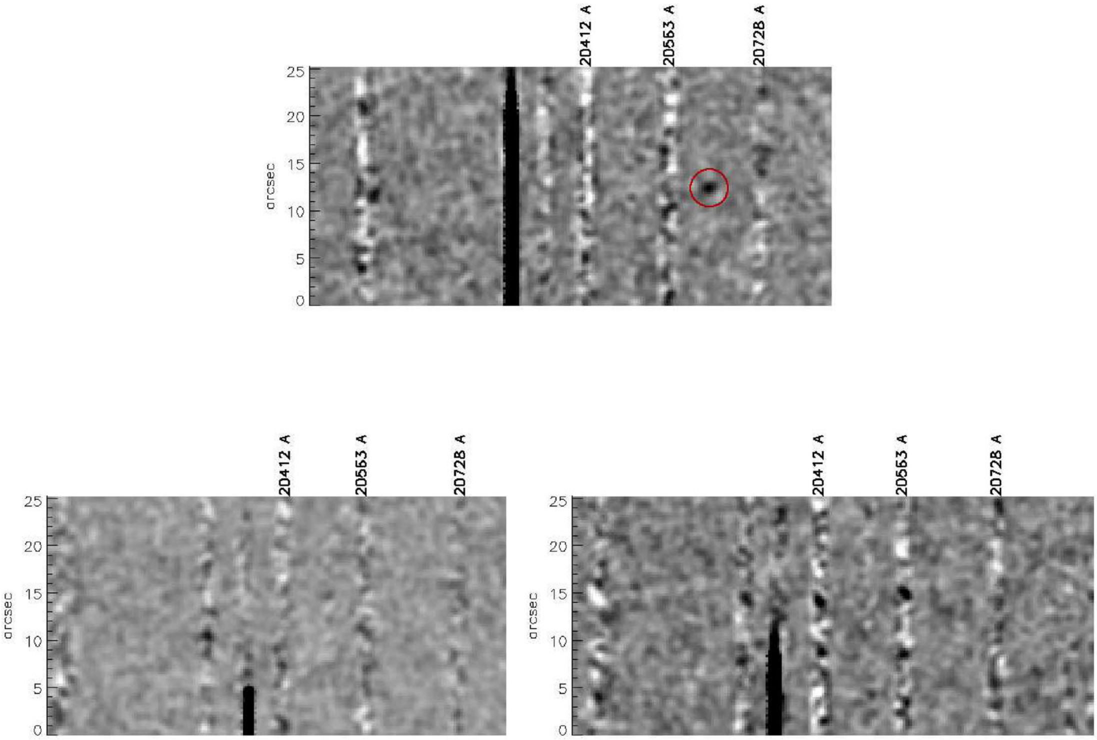

Figure 5. 2D NIR LUCIFER spectra of LAE7745 (top), LAE25972 (bottom left), and LAE6559 (bottom right). Images have smoothed with 3 pixel Gaussian kernel. [O III] detection (5008.24 Å) in LAE7745 highlighted in red circle. A bad column in the detector is seen just left of centre in each frame.

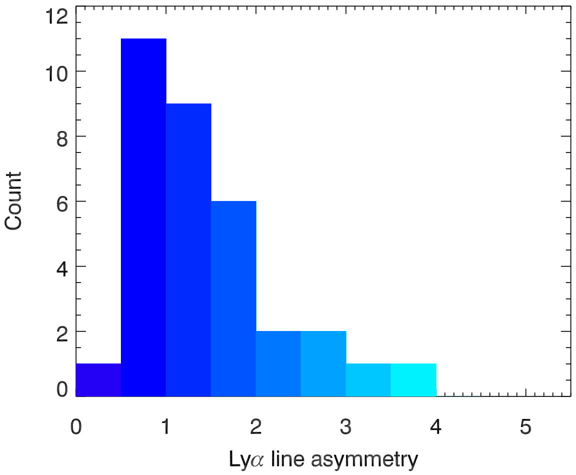

Figure 6. Histogram of Lyα line asymmetry in sample of 33 $z \sim 3.1$ LAEs.

3.2 New [O III] detection

As mentioned above, this paper presents one new [O III] detection in a $z \sim 3.1$ LAE, excluding an [O III] detection in a likely AGN. Our new measurement was made in the same manner as the [O III] line flux measurements in Mc11. Namely, we fit the [O III] line with a symmetric Gaussian plus constant, using the IDL routine MPFITEXPR. The area under the best-fitting Gaussian determines the line flux of the [O III] line, the central wavelength of the fit determines the systemic redshift of the galaxy, and the constant term is the continuum level. We report an error on these measured quantities determined from 1000 Monte Carlo (MC) simulations. In these simulations, the actual 1D spectrum was modified at each point by a Gaussian random amount proportional to the error at that point, and then a Gaussian was fitted to this modified data in each simulation. The standard deviation of the 1000 iterations for each quantity represents 1σ. The errors we report are three times this. Following this procedure, LAE7745 has an [O III] line flux of $13.7 \pm 1.8 \times 10^{-17}$ erg s^{-1} cm^{-2}. This is in addition to the our two previous detections reported in Mc11, where line fluxes of $7.0 \pm 0.3 \times 10^{-17}$ and $35.5 \pm 1.2 \times 10^{-17}$ erg s^{-1} cm^{-2} were reported for LAE27878 and LAE40844, respectively. The other characteristics of the best-fitting Gaussian for LAE7745 are a central wavelength of 20 636.7 ± 1.3 Å, FWHM = 19.7 ± 0.12 Å, and a constant term consistent with zero ($0.9 \pm 1.3 \times 10^{-18}$ erg s^{-1} cm^{-2} Å^{-1}).

We do not detect the second [O III] line at rest-frame 4960 Å in LAE7745. We placed an 3σ upper limit on this line by adding a mock Gaussian emission line to the spectra to represent the 4960 Å line and testing the level to which we could recover it, a procedure similar to that in Finkelstein et al. (2011b). The sigma of the Gaussian was fixed to 12.7 Å which is the best-fitting sigma from the 5008.24 Å line. The line centre was fixed using the redshift of the 5008.24 Å line as well. We then measured the mock line by fitting a symmetric Gaussian using MPFITEXPR, as we would for an actual [O III] detection. The noise on the measurement was determined from 1000 MC iterations, where the flux was modified each time by a random amount proportional to the error bars. We repeated this measurement with decreasing line fluxes until the SNR dropped below 5σ. The line flux where the 5σ threshold was crossed became our 5σ value from which we were able to determine σ and therefore a 3σ line flux detection limit. From this procedure, we determine a 3σ upper limit for this line of 6.9×10^{-18} erg s^{-1} cm^{-2}.

3.3 AGN in the sample

LAE25972 was not well fitted with any of our star-forming SED models, leading to consideration that this object may instead be a

Lyα-selected AGN, especially since this object also had the largest Lyα line flux in our sample. This object does not have an X-ray counterpart in the *Chandra* COSMOS Survey Point Source Catalog (Elvis et al. 2009) but the catalogue may be too shallow to rule out a faint X-ray counterpart (limiting depth $= 5.7 \times 10^{-16}$ erg s^{-1} cm^{-2}, corresponding to X-ray luminosity of 4.9×10^{43} ergs s^{-1} at $z = 3.1$, assuming a X-ray photon index $\Gamma = 2.0$). This object does, however, have a number of other AGN signatures based on the strength of its Lyα line. For example, the Lyα line flux of 7.8×10^{-16} erg s^{-1} cm^{-2} corresponds to a Lyα luminosity of 6.75×10^{43} erg s^{-1}. This Lyα luminosity is larger than five of the six Lyα-selected AGN at $z = 3.1$–3.7 discussed in Ouchi et al. (2008). A comparison to Zheng et al. (2010) yields a similar conclusion – namely Zheng et al. (2010) found that all Lyα detected objects with Lyα luminosity $\geq 1.8 \times 10^{43}$ were AGN. They investigated seven Lyα-selected AGN from $z = 3.1$–4.5 to reach this conclusion. Given the diagnostics from Ouchi et al. (2008) and Zheng et al. (2010), we conclude that this object is likely an AGN.

LAE42795 also does not have an X-ray counterpart in the *Chandra* COSMOS Survey Point Source Catalog, but it does have a very strong, broad [O III] detection. We interpret this as strong evidence for AGN activity in this object. This interpretation is supported by a possible detection of the C IV 1549Å line in the MMT optical spectrum at ~6415.4 Å which agrees with the Lyα- and [O III]-derived redshifts for this object. Finally, the Lyα line in this object is also broad. The red side of the best-fitting asymmetric Gaussian has σ = 11.3 Å, which would correspond to an FWHM of ~1585 km s^{-1}. The left-hand side of the best-fitting asymmetric Gaussian has σ = 5.4 Å, which would correspond to an FWHM ~ 756 km s^{-1}. If we take the average of these FWHM values as the appropriate FWHM for the asymmetric Gaussian, then velocity-width of this Lyα line is ~1170 km s^{-1}.

We exclude both of these likely AGN from our SED fitting results below, and they are excluded anywhere average characteristics of the LAEs are reported, so that these averages only reflect the characteristics of (33) typical star-forming LAEs in our sample.

3.4 Lyα–[O III] velocity offsets

Using the new [O III] detection, we are also able to determine a velocity offset between the Lyα and [O III] lines as we did in Mc11. The [O III] line defines the systemic velocity of the galaxy, and the Lyα line, subject to resonant scattering from neutral hydrogen both in the galaxy and in the IGM as well as dust attenuation, is shifted redwards. We find a velocity offset between [O III] and Lyα in LAE7745 of 52 ± 25.2 km s^{-1}, after correction for the Earth's motion. We follow the same procedure we reported previously in Mc11 to make this new measurement; the velocity offset is determined based by comparing the central wavelength of [O III] and Lyα – where the central wavelength is determined by the best-fitting asymmetric (for Lyα) and symmetric (for [O III]) Gaussians. The offset between the [O III] and Lyα lines is illustrated in Fig. 7 below, mirroring the plots are shown in fig. 2 in Mc11. The measurement reported here is in addition to the velocity offsets of 125 ± 17.3 and 342 ± 18.3 km s^{-1} we previously reported for LAE27878 and LAE40844, respectively, making the new measurement the smallest velocity offset we have seen. This result is suggestive of a wide distribution of velocity offsets in LAEs at $z \sim 3.1$ – suggesting there is not a single characteristic velocity offset but rather a distribution. This diversity of observed velocity offsets is supported by the velocity offsets presented in other samples of $z \sim 2$–3 galaxies where velocity offsets between Lyα and rest-frame optical emission lines are derived (e.g. Finkelstein et al. 2011a; Kulas et al. 2012; Chonis et al. 2013). This result is not surprising considering the generally diverse physical characteristics (age, mass, star formation history, etc.) of the sample that we find from SED fitting in Section 4. If these observed velocity offsets are due to starburst-driven winds, one would expect galaxies with diverse characteristics to drive different winds. We also note that this result is still consistent with the various models (e.g. Verhamme et al. 2006, 2008; Steidel et al. 2010) discussed in Mc11 as possible matches to our observations.

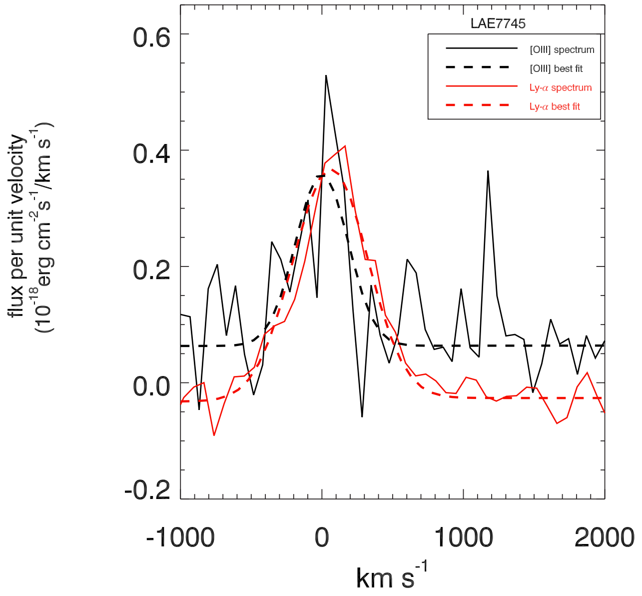

Figure 7. Velocity offset between [O III] and Lyα as detected in one new LAE observed in 2011 with Hectospec and LUCIFER. [O III] spectrum is in black, Lyα spectrum is in red. Lyα line is offset from [O III] by 52 km s^{-1}. See Mc11, Fig. 2, for two previously observed LAEs with velocity offsets of 342 and 125 km s^{-1}.

While detections of [O III] in the NIR for high-z LAEs are still fairly novel, making this an exciting result and one that shed light on the kinematics of LAEs and Lyα escape, we would like to have a better ability to predict which LAEs will yield [O III] detections, since only three of our six observations have yielded [O III] detections so far (excluding the two AGN). A new approach that may help tackle this challenge is discussed in Section 4 below. In addition, more detections are needed to really understand the full distribution of these velocity offsets, and how they correlate with other characteristics of LAEs. This distribution is something we cannot characterize yet with only small samples currently available, but this is becoming more approachable as more NIR instruments come online, particularly those with multi-object capabilities.

4 CONSTRAINING PHYSICAL PARAMETERS WITH SED FITTING

To constrain the physical properties of our 33 (non-AGN) LAEs, we generated stellar population model spectra produced using the updated models of Bruzual & Charlot (2003), which will henceforth be referred to as CB11. This latest version includes contributions from thermally pulsing asymptotic giant branch (TP-AGB) stars and allows for exponentially increasing star formation histories. We use a Salpeter IMF. We created model spectra with an extensive grid of ages, metallicities, star formation histories, and dust extinction values. We also present an additional fitted parameter, a line flux contribution to the K_s band, which is discussed in more detail below. For $z \sim 3.1$ LAEs, the 5008.240 Å [O III] line is redshifted into the K_s filter so this is the line to which we assign the additional flux. We report a single line flux for the [O III] line, but one can consider that this emission is really split between the two lines in the 4960.295/5008.240 Å [O III] doublet (with a ratio of ∼1–3 in the 4960.295 and 5008.240 lines, respectively). Technically, the 4862.683 Å Hβ line also falls in the K_s filter for a $z \sim 3.1$ galaxy, and the 3727.092/3729.875 Å [O II] lines could fall in the H filter. However, our LUCIFER observations have covered the full H and K_s wavelength range, and we have only detected [O III]. Hence, for this work we attribute all the additional line flux in the K_s band to [O III]. We note, however, that our method does not rule out that this emission comes from multiple lines and it could be divided among [O III] and Hβ a posteriori. Because we have not yet detected [O II] we do not alter the H-band flux for this line, but this could easily be added to future analyses if future observations indicate that it is warranted. It is also worth noting that most SED results to date have indicated LAEs are relatively metal poor (e.g. Finkelstein et al. 2011b; Nakajima et al. 2013), and hence we can expect the [O III] line to be much brighter and contribute much more to the broad-band flux than the [O II] lines.

Ages for our models vary on an irregular grid of 48 values, from 2 Myr to 2 Gyr (approximately the age of the Universe at $z = 3.1$). Dust extinction, $E(B-V)$, is allowed to assume 31 regular values to produce 0–6.6 mag of dust extinction (A_{1200}). Dust attenuation is applied to our models using the Calzetti formulation (Calzetti et al. 2000). Metallicity is allowed to assume five values from 0.005 to 1.0 $Z_\odot$. We chose only exponential star formation rates, investigating both exponentially increasing and exponentially decreasing rates. Star formation history e-folding time, τ, can assume six positive values from $\tau = 0.0001$ to 4.0 Gyr. This essentially creates one template of instantaneous star formation (when $\tau = 0.0001$ Gyr which is much younger than the age of the O/B star) and one template with continuous star formation (when $\tau = 4$ Gyr which is longer than the age of the Universe at $z = 3.1$) with four templates of exponentially decaying star formation in between ($\tau = 0.001$, 0.01, 0.1, 1 Gyr). We add to this two negative e-folding times ($\tau = -0.1$, -1 Gyr) to explore exponentially increasing models due to recent results (Maraston et al. 2010; Finlator, Oppenheimer & Davé 2011; Papovich et al. 2011) that have indicated high-z LAEs may be better fitted with exponentially increasing star formation rates. This brings our total number of possible τ values to eight. Redshifts were fixed for each object, depending on the redshift of the Lyα line, as this should be close to the correct redshift depending on the possible velocity offset of Lyα from systemic (even with our largest detected offset of 342 km s^{-1} in Mc11, δz between Lyα and [O III] is <0.005). Our full grid contains 1.116×10^6 models, probing a very large parameter space.

4.0.1 Photometry for χ^2 Minimization

For our SED fits, we used model and observed photometry in the B, r', i' z', J, H, and K_s, bands and IRAC 3.6 μm bands. We use photometry from the COSMOS Intermediate and Broad Band Photometry Catalog (Capak et al. 2007) for the B, r', i', and z' bands (3 arcsec aperture photometry). We do not use the u^* filter because this is the dropout band for $z \sim 3.1$ LAEs. The g' band is not used since the redshifted Lyα line is centred in this filter. The V band is excluded for a similar reason, as the filter has transmission between 55 and 65 per cent at the location of the Lyα line. The IRAC 3.6 μm data come from the S-COSMOS IRAC 4-channel Photometry Catalog[8] available on the NASA/IPAC archive. We use the 2.9 arcsec aperture fluxes from this catalogue (Sanders et al. 2007). Six LAEs have IRAC 3.6 μm detections in this catalogue. For uncrowded objects with no IRAC 3.6 μm detection, we use the 3σ depth (0.54 μJy) of the IRAC 3.6 μm image for the observed data point. This is the case for 15 LAEs. In the 12 cases where neither a detection nor an upper limit could be used, the χ^2 minimization process does not use an IRAC 3.6 μm point. 29 of the LAEs in our sample are covered by the deep UltraVISTA Survey in the COSMOS field (McCracken et al. 2012), and we used these new J, H, and K_s images (Data Release 1) for our NIR photometry. The photometry for each object was measured using SExtractor. SExtractor detections were forced at the desired coordinates (coordinates taken from the COSMOS catalogue) by creating images with bright, fake sources at the correct coordinates and running SExtractor in dual-image mode with these fake images as the detection images and the $J/H/K_s$ images as the measurement images. For the four LAEs not covered by UltraVISTA, we extracted J, H, and K_s photometry from earlier publicly available COSMOS images. We used the CFHT H and K_s band images (McCracken et al. 2010) and for J we used the UKIRT J images (Capak et al. 2007). Again, SExtractor detections were forced at the desired coordinates as described above, in 3 arcsec apertures, error bars UltraVISTA and COSMOS NIR data are taken directly from SExtractor.

4.1 SED models

The CB11 code creates model spectra in units $L_\odot\ A^{-1}$ for $\lambda = 91$–3.6×10^8 Å. This output was converted to flux density (F_ν) using the following two conversions (Papovich, Dickinson & Ferguson 2001):

$$L_\nu = \frac{10^8 \lambda_0^2 l_\lambda L_\odot}{c M_{\rm gal}} 10^{-0.4[E(B-V)k'(\lambda)]} \qquad (13)$$

$$F_\nu = \frac{(1+z)L_\nu}{4\pi d_L^2} {\rm e}^{-\tau_{\rm IGM}}. \qquad (14)$$

Here, l_λ is the CB11 output in units $L_\odot A^{-1}$, 10^8 converts from Å to μm, $[E(B-V)k'(\lambda)]$ is wavelength dependent and calculated from Calzetti et al. (2000), λ_0^2 is wavelength in the galaxies rest-frame, $M_{\rm gal}$ is the total mass in the stellar population at a given age (which results in the spectrum being normalized to 1 $M_\odot$), z is the redshift of the model, fixed to $z = 3.1$, $\tau_{\rm IGM}$ is wavelength-dependent IGM absorption from Madau (1995) and $d_{\rm L}$ is the luminosity distance for $z = 3.1$. After the application of equation (14) and convolution of the flux through each filter, we have an individual flux density value for each filter (B, r', i', z', J, H, K_s IRAC 3.6 μm).

It is at this point that we add our new parameter, [O III] line flux. We modify (amplify) the flux in the K_s band to mimic how [O III] can contribute flux in this filter. The modification looks like

$$f_{\rm total} = f_k + f_{\rm [O\,III]}, \qquad (15)$$

where f_k is the unmodified model flux density in the K_s band. $f_{\rm [O\,III]}$ is the [O III] line flux in the band, and $f_{\rm total}$ is the total flux density in the K_s band after those of two fluxes are combined. $f_{\rm [O\,III]}$ is defined as

$$f_{\rm [O\,III]} = x f_k, \qquad (16)$$

---

[8] http://irsa.ipac.caltech.edu/data/COSMOS/tables/scosmos/

where x takes on 15 uniform values from 0 to 1.5, meaning there are 15 possible [O III] fluxes that could be fit. When $x = 0$ this means there is no additional line flux from [O III] added to the K_s band, and this result is chosen as the best fit for some of our LAES (see Section 5). This method essentially allows for additional line flux in the K_s band, but allows the underlying spectrum to still be a younger/less massive galaxy, which would not necessarily be the case if an artificially large K_s-band flux forced an older and more massive solution to be fit. Schaerer & de Barros (2009) pointed out the importance of including some treatment of nebular emission lines when fitting starbursting galaxies, when they found that ages in a sample of $z \sim 6$ galaxies could be overestimated by as much as four times and mass by as much 1.5 times when nebular emission lines were not accounted for. Some treatment of nebular emission lines is certainly warranted, but we advocate for a simple methodology (equation 15) for accounting for nebular emission. This methodology only requires that a single additional parameter be added to our fitting process, avoiding a complex recipe of adding a large number of lines to our spectra – and this single parameter can be accounted for across all possible star formation histories and metallicities. As Nilsson et al. (2011) and Nakajima et al. (2012) have noted, accounting for such detailed nebular emission line recipes across multiple star formation histories and metallicities can be too complex, limiting the parameter space that can be probed. We avoid this by dealing with only a single parameter that is matched to what we have actually observed – i.e. we have observed some of these LAEs in the NIR and only detected [O III], so this is the only line/parameter we are adding. Additionally, we can directly compare our NIR observations to the predictions from our model fitting process (see Section 6.1).

Finally, mass is a fitted parameter, calculated from minimizing the χ^2 in equation (17) for each model. This means that for each model there is a single best-fitting mass solution found by minimizing χ^2 with respect to mass:

$$\chi^2 = \sum_i \left[\frac{f_{\nu,i}^{\mathrm{obs}} - M f_{\nu,i}}{\sigma_i} \right]^2 . \tag{17}$$

Here the subscript 'i' represents each filter where the model and observed photometry are compared.

4.2 Allowed fits

Some of our LAEs are best fit, strictly via χ^2 minimization, with old stellar populations. These fits require careful consideration because older stellar populations may not be able to produce enough ionizing photons to produce the Lyα lines we have measured (with optical spectroscopy) in these objects. We therefore consider some additional constraints on these objects to see if these old best-fitting solutions are, in fact, realistic, physically motivated solutions or if they ought to be ruled out in favour of younger, dustier solutions.

The CB11 code produces a parameter, NLyc, that is the log rate of ionizing photons (s^{-1}) produced at each age of the model for a given metallicity. Assuming case B recombination, where two of every three of these ionizing photons produce a Lyα photon, we can turn this production rate into a Lyα line strength at each model age. This allows us to test if the best-fitting age for a given object is able to produce, at a minimum, the Lyα line we have measured for that object with spectroscopy. We do not subject this Lyα line to attenuation by dust and/or the IGM, as we are simply testing if, at a minimum, the model stellar population could intrinsically produce enough ionizing photons to begin with, before any attenuation.

The actual mechanism for this calculation is as follows:

$$\mathrm{Ly}\alpha \text{ line flux} = \frac{2}{3} \frac{10^{\mathrm{NLy}\alpha}[h\nu_{\mathrm{Lyc}}]}{4\pi d_{\mathrm{L}}^2} \frac{M_m}{M_{\mathrm{gal}}}, \tag{18}$$

where $\frac{2}{3}$ is the coefficient for Lyα for case B recombination, NLyc is the log production rate of ionizing photons, $h\nu_{\mathrm{Ly}\alpha}$ is the energy of a Lyα photon, and d_{L} is the luminosity distance at $z = 3.1$ (Wright 2006). M_{gal} is the total mass in the stellar population at a given age and M_m is the best-fitting mass (in $\mathrm{M}_{\odot}$) for the model under consideration, so that the final term $\frac{M_m}{M_{\mathrm{gal}}}$ scales the model stellar population from its normalized, $<1\ \mathrm{M}_{\odot}$ mass, to the appropriate galactic size stellar mass.

Only models (i.e. combinations of metallicity, age, star formation history, dust, and mass) that can produce, at a minimum, enough ionizing photons to power the Lyα line we observe are considered 'allowed' fits. With this information, we find the model with the smallest χ^2 from among only these 'allowed' possibilities. Henceforth, we will refer to this as the best allowed-fit for each object. Consequently, the best allowed-fit solution is not always the model with the absolute smallest χ^2.

An example of this calculation, for LAE40844, is shown in Fig. 8. Fig. 8 shows the strength of the Lyα line (solid curve) as function of stellar populations of increasing age for constant mass, metallicity, and τ. This particular figure is constructed using the best allowed-fit model for LAE40844, where metallicity is 0.2 $\mathrm{Z}_{\odot}$, τ is 0.001 Gyr, and mass is $2.9 \times 10^9\ \mathrm{M}_{\odot}$. The maximum age this combination of mass, metallicity, and τ can have and still produce the amount of Lyα flux we have observed is shown as a black vertical line. The best allowed-fit age is shown as a red vertical line. This diagnostic shows why this combination of mass, τ, metallicity, and age is an allowed solution for LAE40844 – namely that the model age is to the left (younger) than the maximum age allowed that could still produce the number of Lyα photons we have observed from this object. The observed Lyα line strength is shown as a dashed line.

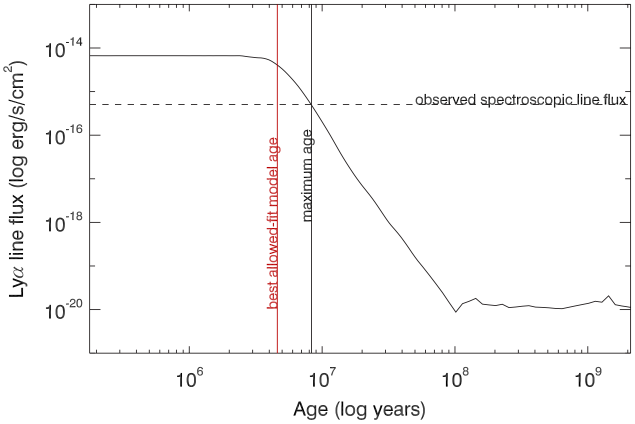

Figure 8. Model Lyα line flux (solid curve – from equation 18) that can be produced by stellar populations of increasing age, for a fixed mass, metallicity, and star formation history. This is the best allowed-fit model for LAE40844, where metallicity is 1 $\mathrm{Z}_{\odot}$, τ is 0.01 Gyr, and mass is $2.17 \times 10^9\ \mathrm{M}_{\odot}$. The horizontal dashed line shows the observed spectroscopic Lyα line flux for LAE40844. The age of the best allowed-fit model is the red vertical line, where only models younger than the black vertical line can produce the observed Lyα line flux.

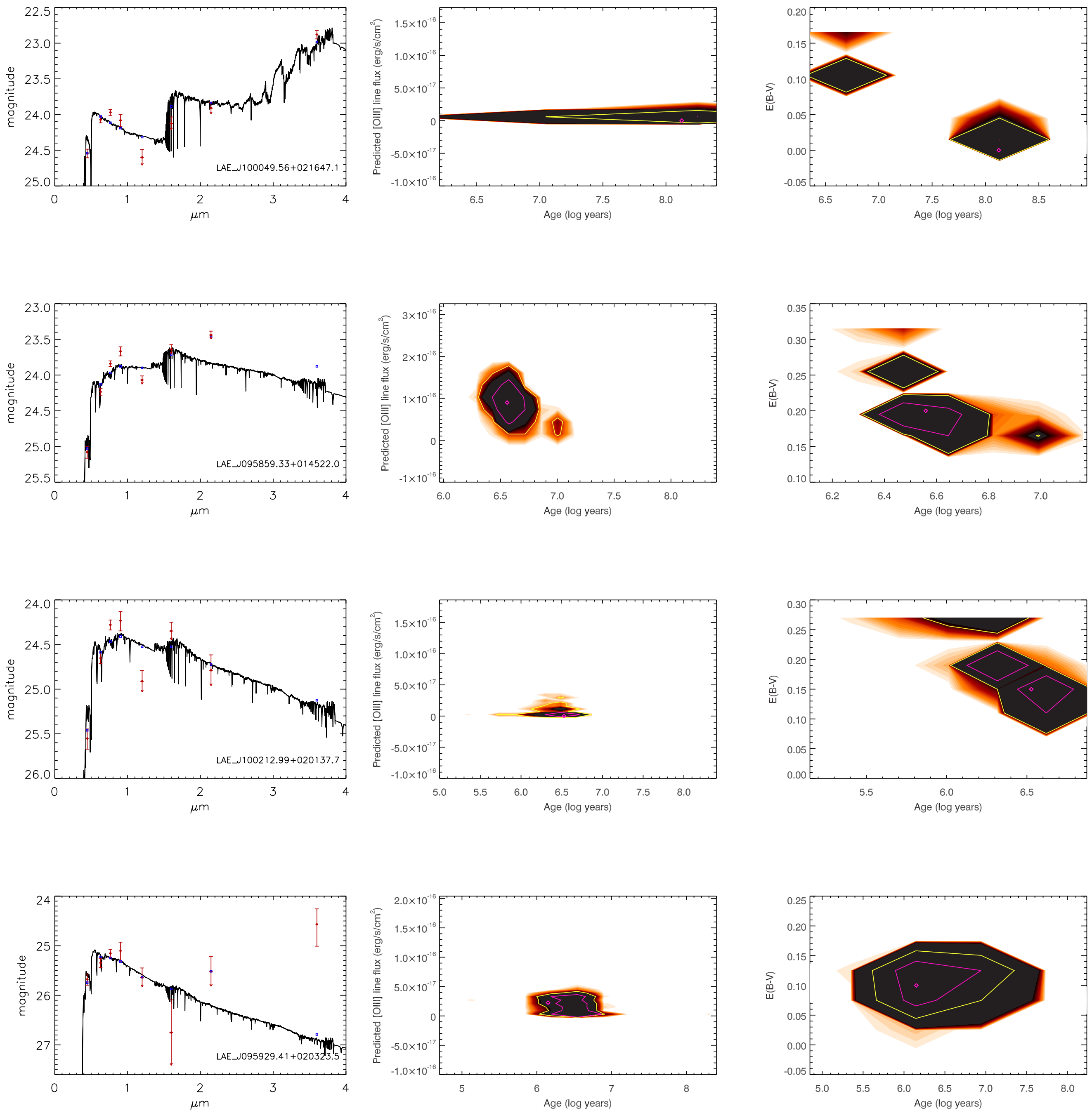

Figure 9. The first column contains the best allowed-fit model spectra for the first four LAEs. Model spectrum is black, model magnitudes are shown as blue squares. Observed magnitudes are shown as red diamonds. Red diamonds with a downward arrow instead of error bars indicates that an observed point was fainter than the 3σ depth. Plotted magnitudes are in B, r', i' z', J, H, K_s, and IRAC 3.6 µm, from left to right. Large error bars in V and g' bands are sometimes a consequence of subtracting the Lyα line from these filters. The second and third columns show density plots from our MC simulations. Ages shown here are star formation weighted ages. The best allowed-fit is shown as a magenta diamond. Contours encompassing ∼ 68 and ∼ 95 per cent of the results are shown in magenta and yellow, respectively. The order of objects in Fig. 9–15 matches the order of objects in Tables 2 and 3. AGN are excluded from both table and figures.

5 RESULTS FROM SED FITTING

We find a diverse spread of physical characteristics from SED fitting for our sample of 33 LAEs. Detailed descriptions of each physical characteristic are described in Sections 5.2–5.6 below. The authors note that some of the diversity in physical characteristics is certainly real, some of it may arise from the iterative nature of our selection process that was used to build this sample (see Section 2.3). Model spectra are shown below in Figs 9–15 for all 33 LAEs. Observed magnitudes are shown as red diamonds and error bars on observed photometry are also shown. Red diamonds with a downward arrow instead of error bars indicates that an observed point was fainter than the 3σ depth of that band. Magnitudes from the model spectra are shown as blue diamonds. For objects where the model included [O III] line flux in the K_s band, you will note that both the red and blue diamonds lie above the black model

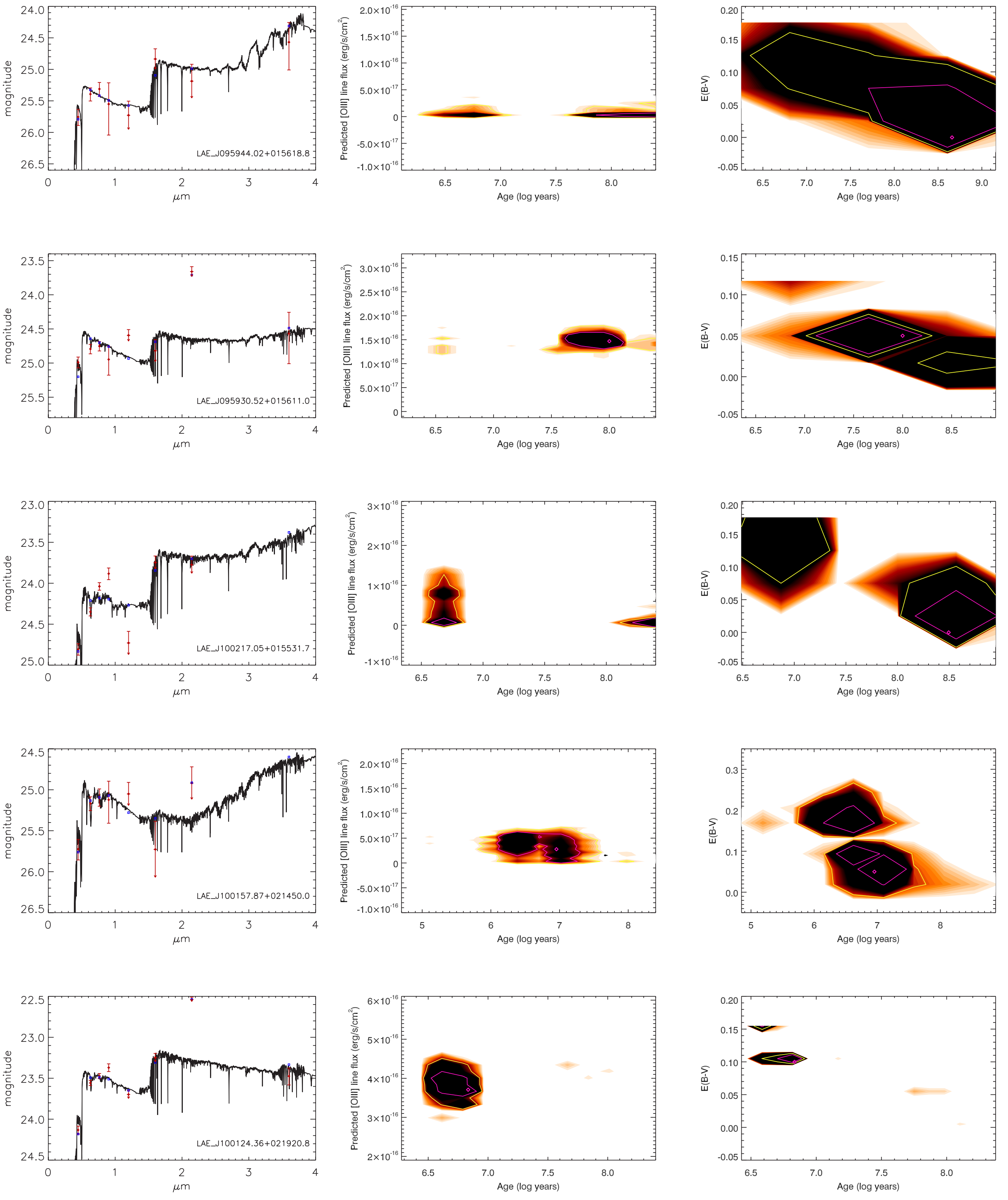

Figure 10. Same as Fig. 9 for next five objects.

spectrum. This is expected as it means that an artificially large K_s-band flux from [O III] line flux pollution in this band is not dominating/skewing the best-fitting results. Results for fitted parameters for each object are shown in Tables 2 and 3 along with 68 per cent confidence intervals for each parameter. Plots of age versus mass, [O III] line flux versus age, metallicity versus age, and $E(B-V)$ versus age are shown in Figs 16 and 17 for the population of 33 LAEs.

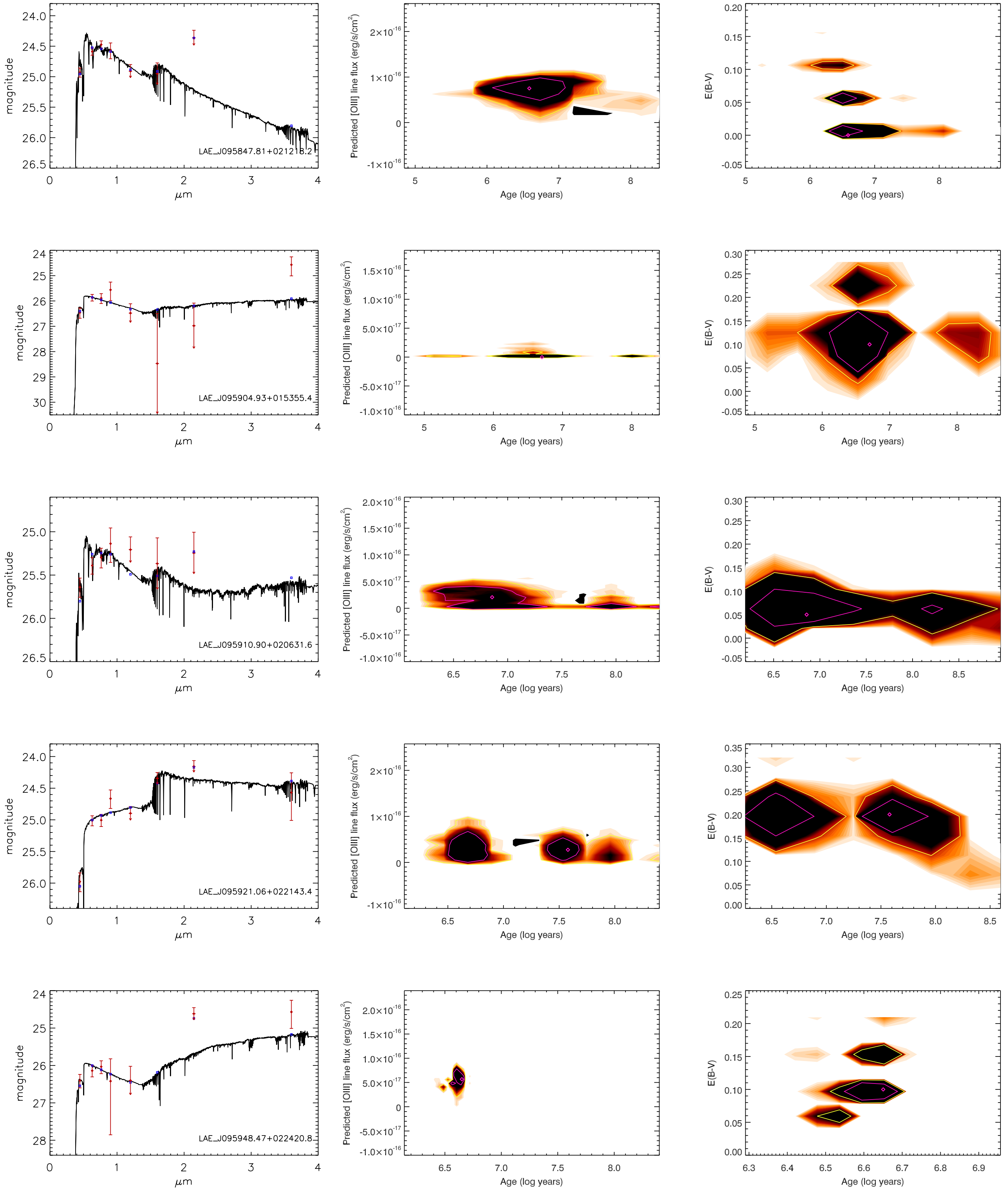

Figure 11. Same as Fig. 9 for next five objects.

5.1 Goodness of fits

Our median reduced χ^2 is 7.0. The best-fitting object has a reduced χ^2 of 0.9 and the worst fit object has a reduced χ^2 of 48.3. This particular object is one that may have multiple components in the *HST* image (see Section 2.5), which may contribute to the large χ^2 value. We also remind the reader that the model chosen as the best fit is not always the smallest χ^2 solution for each LAE, but rather, the model with smallest χ^2 from among those models that can produce enough ionizing photons (best allowed-fit). For objects with IRAC

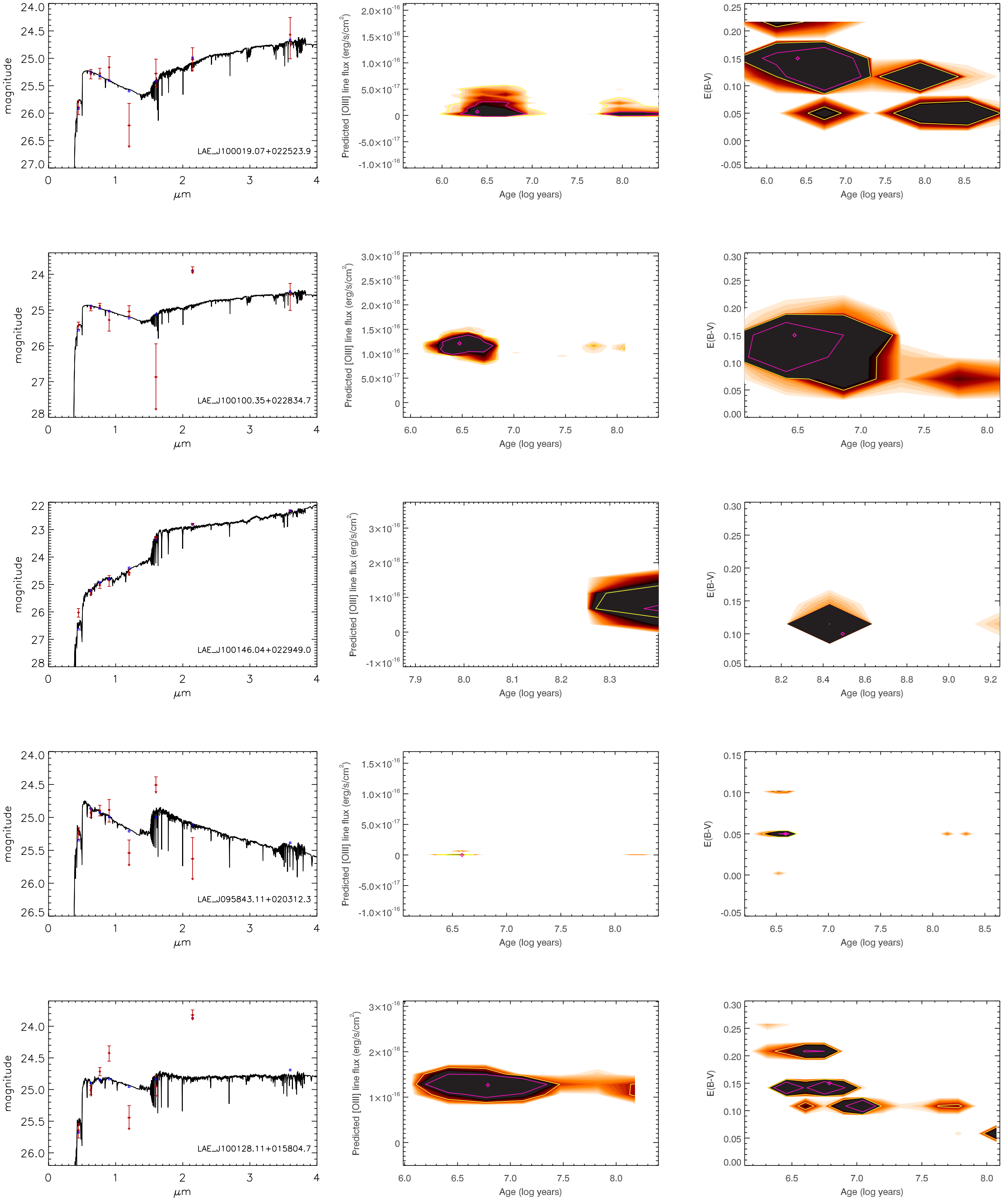

Figure 12. Same as Fig. 9 for next five objects.

3.6 μm photometry (meaning either a detection or the limit was used), there are two degrees of freedom. For objects with no IRAC 3.6 μm data, there is one degree of freedom. These values comes from leveraging eight bands (*B*, *r*, *i*, *z*, *J*, *H*, K_s IRAC 3.6 μm) or seven bands when no data are available for the IRAC 3.6 μm band, against six fitted parameters (age, mass, metallicity, dust, τ, [O III]).

We demonstrated how well constrained the fits are for each LAE with MC simulations of each individual object. We ran 1000 MC

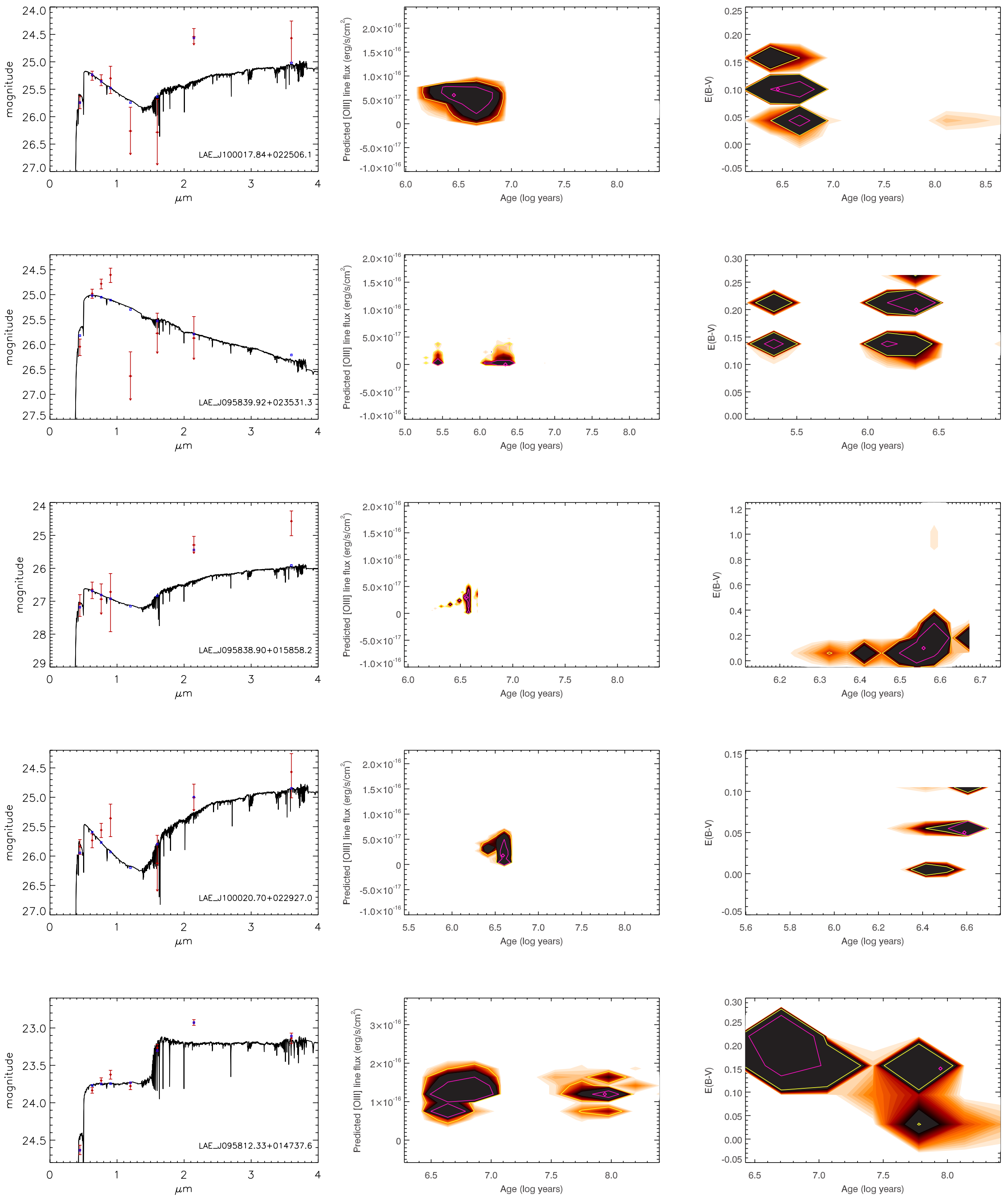

Figure 13. Same as Fig. 9 for next five objects.

simulations for each object. In each of the 1000 iterations, we modified the observed fluxes in each band by a Gaussian random amount proportional to the error bar in that band and then we determined the best allowed-fit model for the altered photometry in the same manner as described above. Density plots showing the distribution of MC solutions around the best fit are shown in Figs 9–15 for age, predicted [O III] line flux, and dust. Similar plots for additional fitted parameters are included in Appendix A (online

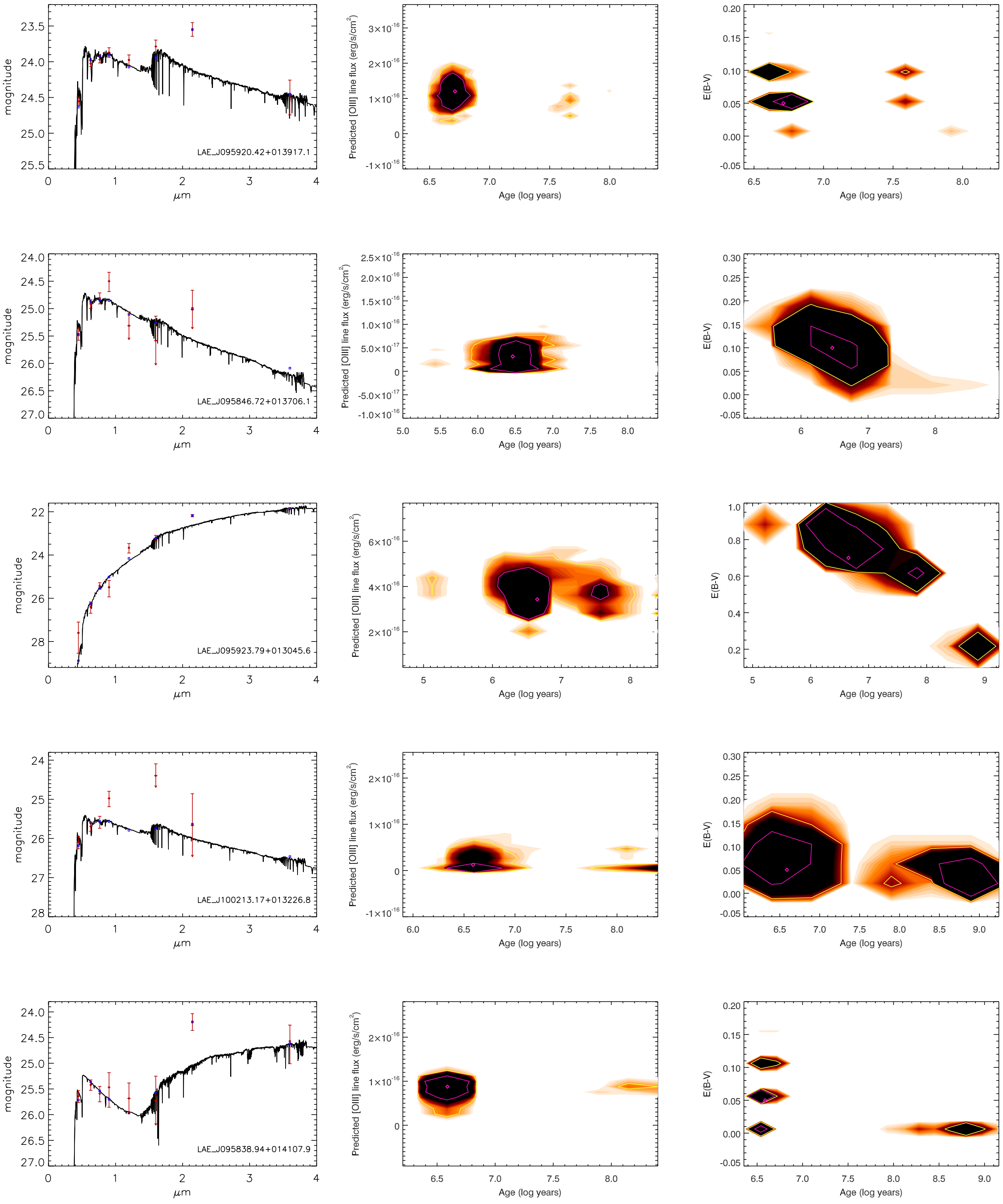

Figure 14. Same as Fig. 9 for next five objects.

only). Contours encompassing approximately 68 and 95 per cent of the MC results are also shown on each plot. In addition, Tables 2 and 3 list these 68 per cent confidence ranges for each fitted parameter. This range was calculated by sorting (from smallest to largest) the 1000 MC solutions for a given parameter, and finding the spread given by the central 680 solutions in the sorted array. The error bars reported below on any model predictions are derived from this 68 per cent confidence range.

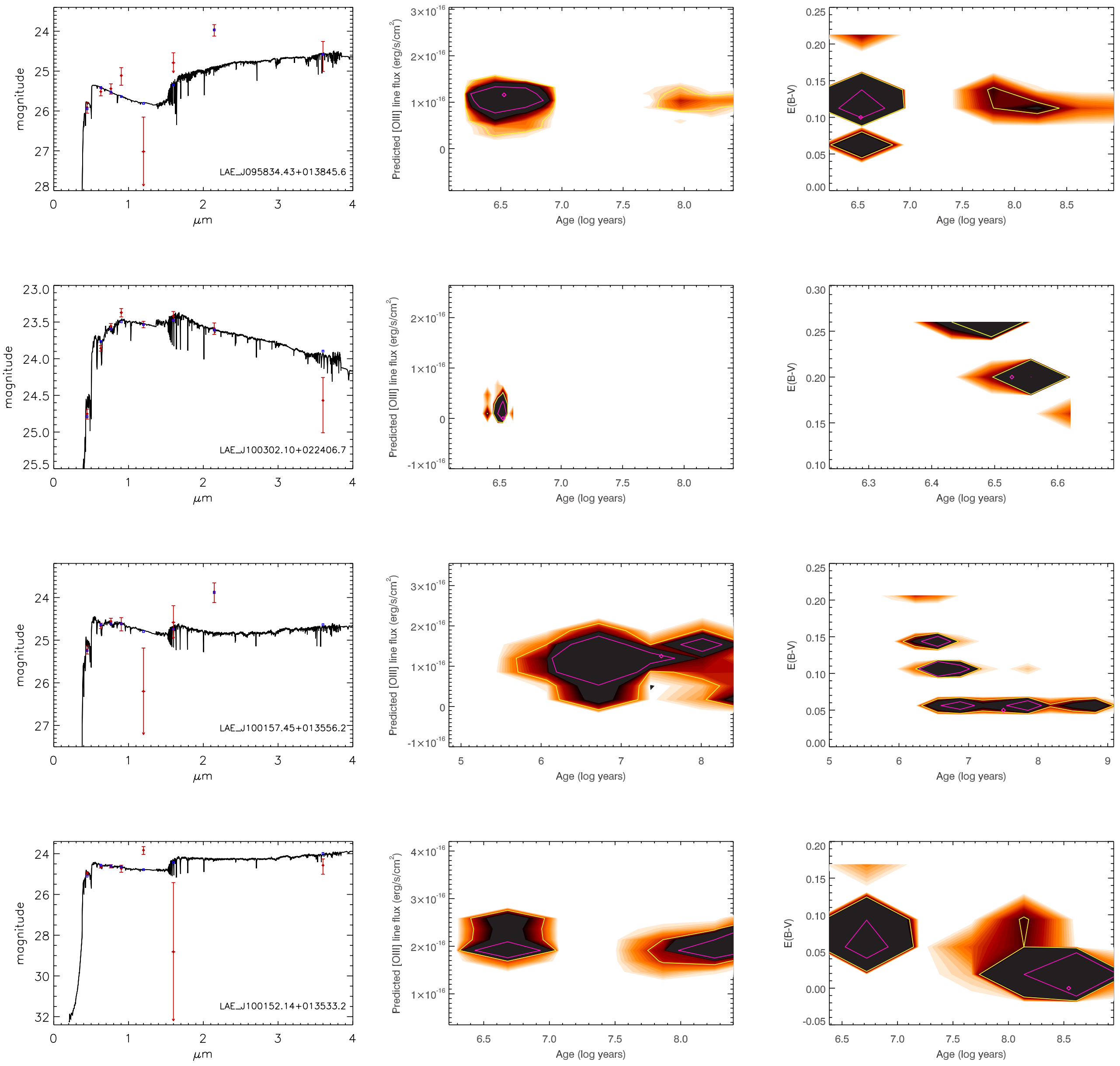

Figure 15. Same as Fig. 9 for next four objects.

5.2 Star formation history results

While some recent literature (Maraston et al. 2010; Finlator et al. 2011; Papovich et al. 2011) has suggested that, on average, high-z star-forming galaxies may be better fitted with exponentially increasing star formation rates, in fitting 33 individual LAEs we find that only four galaxies in our sample are best fit with an exponentially increasing star formation rate. Instead, we find that the majority of the sample is best fit with a single instantaneous burst (48 per cent, $\tau = 0.0001$ Gyr) or exponentially decreasing star formation rates (39 per cent, $\tau = 0.001 - 1.0$ Gyr). No LAEs in our sample are best fitted with constant star formation rates ($\tau = 4$ Gyr).

5.3 Age results

We report star formation rate weighted ages, age$_{\rm SFR}$, for each galaxy both here and in Tables 2 and 3. Star-formation-weighted ages better represent the age of the bulk of the stars and are therefore more informative than directly quoting the ages of the models. Equation (19) shows the derivation of this weighted age for exponentially decreasing star formation rates (Raichoor et al. 2011)

$$\langle {\rm age}\rangle_{\rm SFR} = \frac{\int_0^t (t-t')e^{-t'/\tau}dt'}{\int_0^t e^{-t'/\tau}dt'} = \frac{\tau e^{-\frac{t}{\tau}} - \tau + t}{1-e^{-\frac{t}{\tau}}}, \qquad (19)$$

where t is the age output from the model (i.e. time since star formation began) and τ is the e-folding time of the star formation rate as output from the model. We also derived the same type of star-formation-weighted age for the case of exponentially increasing star formation, with the expression shown as follows:

$$\langle {\rm age}\rangle_{\rm SFR} = \frac{\int_0^t (t-t')e^{t'/\tau}dt'}{\int_0^t e^{t'/\tau}dt'} = \frac{\tau - \tau e^{\frac{-t}{\tau}} - te^{\frac{-t}{\tau}}}{1-e^{\frac{-t}{\tau}}}. \qquad (20)$$

Our median age$_{\rm SFR}$ is 4.5×10^6 yr, with age$_{\rm SFR}$ results spanning 1.4×10^6–4.6×10^8 year. The median size of the 68 per cent confidence ranges calculated for each object is 3.2×10^6 yr.

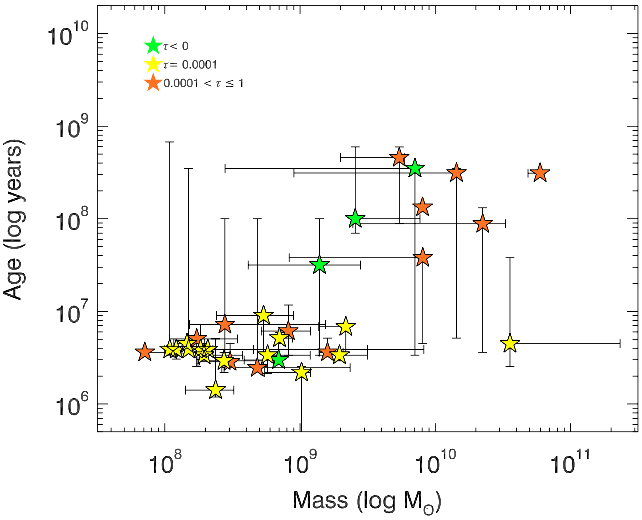

Figure 16. The distribution of age$_{\mathrm{SFR}}$ versus mass for various τ values for 33 LAEs. Green stars indicate models with exponentially increasing star formation rates ($\tau < 0$), yellow stars are fits with a single instantaneous burst ($\tau_{\mathrm{SFR}} = 0.0001$ Gyr), and orange stars are those with exponentially decaying star formation rates. Since mass and age parameters are correlated this plot is mainly meant to illustrate and confirm the distribution of τ_{SFR} with these parameters, showing that the oldest and most massive LAEs are those fit with increasing star formation rates, the youngest and least massive galaxies are fitted with instantaneous star formation histories, and those LAEs with exponentially decaying star formation rates lie between those two populations.

A majority of our sample (85 per cent) have age$_{\mathrm{SFR}}$ < 100 Myr. Hence, our sample of 33 galaxies fits with previously reported results (e.g. Gawiser et al. 2007; Pirzkal et al. 2007; Finkelstein et al. 2009, 2011a; Cowie et al. 2011) that LAEs have largely young to intermediate ages.

5.4 Stellar mass results

The median stellar mass in our sample is 6.9×10^{8} M$_{\odot}$, the mean value is 5.4×10^{9} M$_{\odot}$. The most massive solution in our sample is 6.0×10^{10} M$_{\odot}$ and the smallest solution is 7.1×10^{7} M$_{\odot}$. The large number of galaxies (14 of 33) that have masses $\geq 1 \times 10^{9}$ M$_{\odot}$ is a result of the wide-field and therefore shallower nature of our survey, meaning we have selected LAEs from the brighter and more massive end of $z \sim 3.1$ LAE population. We discuss this further in Section 6.3.

5.5 Dust results

The median $E(B - V)$ value in our sample is 0.10, corresponding to less than a magnitude of extinction at $\lambda = 1200$ Å. 52 per cent of the sample has 68 per cent confidence ranges that include this median value. The largest $E(B - V)$ value in the sample is 0.7. Only five objects are fitted with absolutely no dust extinction, but an additional three objects have 68 per cent confidence ranges that include $E(B - V) = 0$. We also note that a total of 27 per cent of the sample has the smallest non-zero $E(B - V)$ solution, where $E(B - V) = 0.05$. These trends seem to indicate that overall, we are looking at a sample of galaxies that do not contain much dust.

5.6 [O III] line fluxes results

The main feature that distinguishes this work from previous SED fitting work with LAEs is the inclusion of an additional fitted parameter to account for [O III] line flux in the K_{s} band (where the K_{s} band encompasses the [O III] 5008.240 Å for $z \sim 3.1$ galaxies). We chose to add this single line as this is the only rest-frame optical emission line we have detected in $z \sim 3.1$ LAEs via NIR spectroscopy. This puts us in a unique position to compare [O III] predictions from our models for these three objects with actual measurements in the same objects. We also have three LAEs in which NIR observations

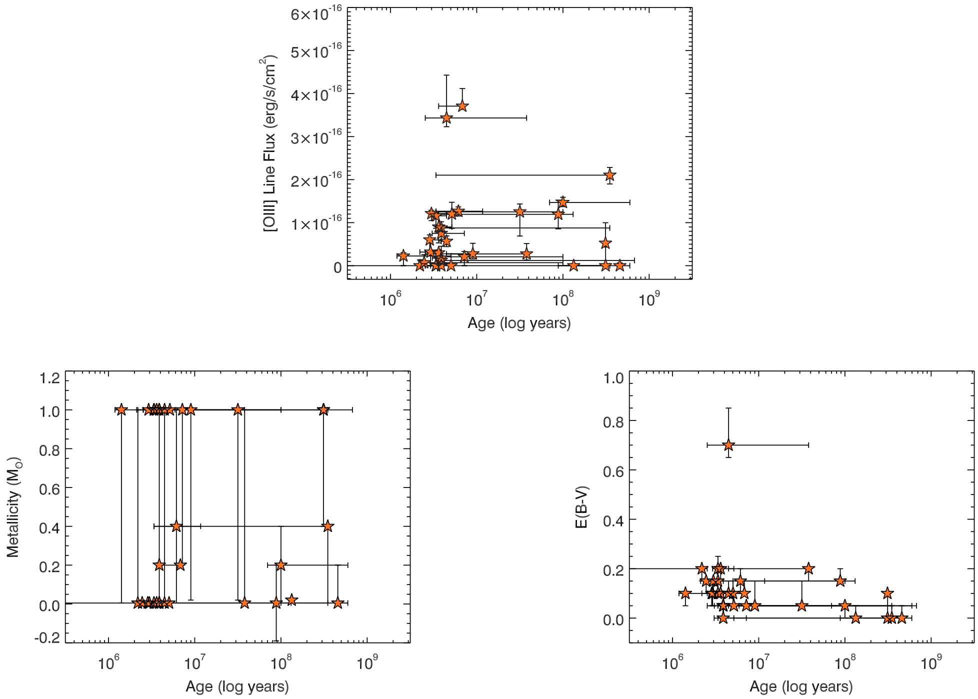

Figure 17. Top plot shows distribution of [O III] line flux versus age. Bottom panel shows similar distributions for metallicity versus age (left), and $E(B - V)$ versus age (right). All ages plotted here are star-formation-weighted ages.

yielded non-detections. As for overall results of our [O III] fitting approach, we find that 76 per cent of our sample is best fitted with an [O III] line flux >0. This means that eight LAEs are best fitted with no additional flux from the [O III] line contributing to the K_s band. The average best-fitting [O III] line flux in our sample is 9.7×10^{-17} erg s^{-1} cm^{-2} (calculated only among the 25 galaxies with non-zero solutions).

6 DISCUSSION

6.1 Comparison of predicted to observed [O III] line flux

We have observed six non-AGN objects with NIR spectroscopy to look for [O III] and other rest-frame optical nebular emission lines. As discussed previously, we have [O III] detections for three of these objects. Comparing [O III] line flux predictions from our model predictions to the actually observed line fluxes, we find that all three of the galaxies with observed [O III] lines select models with [O III] lines. Our best prediction is for LAE40844, in which we observed a line flux of $3.6 \pm 0.1 \times 10^{-16}$ erg s^{-1} cm^{-2} and our model predicted $3.7^{+0.41}_{-0.08} \times 10^{-16}$ erg s^{-1} cm^{-2}; an error between the observation and prediction of less than 3 per cent. The observed [O III] line flux contributes 53 per cent contributes of the observed flux in the K_s for this object; the predicted [O III] line flux contributes 54 per cent. This prediction also lies within the 1σ error bar on the observed [O III] line. In LAE7745, the per cent difference between the observed line flux (1.4×10^{-16} erg s^{-1} cm^{-2}) and the predicted [O III] line bflux ($1.5^{+0.12}_{-0.1} \times 10^{-16}$ erg s^{-1} cm^{-2}) is also small, at ∼7 per cent. In this case, the observed [O III] line contributes ∼ 61 per cent of the flux in the K_s filter, where the model prediction is that ∼ 65 per cent of the flux in the K_s ifilter comes from [O III]. The model prediction for LAE27878 provides the worst agreement. The model prediction is only $0.7^{+1.9}_{-0.7} \times 10^{-17}$, while the observed line flux in this object is $7 \pm 0.3 \times 10^{-17}$. In this object, the observed [O III] line contributes ∼100 per cent of the flux in the K_s filter, whereas the model only predicts a contribution of 10 per cent. The agreement is not good, but it is worth noting that LAE27878 has the smallest [O III] line flux of the three line fluxes we have measured to date, and the model correspondingly assigns the smallest predicted line flux of the 3 to this object as well.

As for the three LAEs in which we detected no [O III] line flux (LAE14310, LAE6559, and LAE27910), our models predict very little [O III] emission ($2.1^{+1.2}_{-2.1} \times 10^{-17}$, $2.3^{+0.7}_{-2.3} \times 10^{-17}$, $6.0^{+1.2}_{-3.0} \times 10^{-17}$ erg s^{-1} cm^{-2}, respectively). This corresponds to predicted contributions to the flux in the K_s filter (of ∼ 34, 50, and 50 per cent, respectively). While the agreement between observations and predictions does not initially seem very good for these objects, we note that the 68 per cent confidence ranges for the [O III] line flux predictions (reported in Tables 2 and 3) in LAE14310 and LAE6559 include zero (i.e. no [O III] line flux). Additionally, while these objects did not have [O III] detections in our LUCIFER or NIRSPEC data, the predicted line fluxes are quite modest. The predicted fluxes for LAE14310 and LAE6559 are the fourth and fifth faintest predicted line fluxes among the 25 models with predicted line flux ≠ 0. We derive a 3σ line flux limit from the 28 min LUCIFER spectrum of LAE6559 of $\sim 1.4 \times 10^{-16}$ erg s^{-1} cm^{-2}. So the predicted model line flux of 2.3×10^{-17} erg s^{-1} cm^{-2} is well below what we would have been able to observe in this object. Given that this same object was also observed with NIRSPEC using a similar 30 min integration which also yielded no detection, we argue that this upper limit should also approximate the upper limit for LAE27910, which was also observed for 30 min with NIRSPEC and which also yielded no detection. Comparison of the model prediction for LAE27910 (6.0×10^{-17} erg s^{-1} cm^{-2}) and this approximate upper limit (1.4×10^{-16} erg s^{-1} cm^{-2}) once again shows that even if the galaxy produced the predicted [O III] flux, we would see it as a non-detection given our modest integration time. For LAE14310, which had a noisier NIR spectrum, we derive a 3σ upper limit of $\sim 2.8 \times 10^{-16}$ erg s^{-1} cm^{-2}, again well above the line flux predicted for this object of 2.1×10^{-17} erg s^{-1} cm^{-2}. Most importantly, these upper limits tell us that there is really no big disagreement between our observed non-detections and our model predictions of a very faint [O III] line.

To compute the 3σ line flux upper limits quoted above, we added and recovered mock Gaussian emission lines following the procedure described in Section 3.2. For the three [O III] line flux upper limits calculated here, we fixed the sigma of the Gaussian to 5.52 Å, or the σ from our faintest [O III] detection (LAE27878). Because it is impossible to know a priori exactly how much the Lyα line is offset from the [O III] line, we had to repeat these calculations, fixing the mock line at different wavelengths to recreate different velocity offsets. We found the 3σ line flux detection limit at 11 different wavelengths for each object, corresponding to velocity offsets of 0–500 km s^{-1}, in increments of 50 km s^{-1}. This range of velocity offsets was chosen to encompass the magnitude of Lyα–[O III] velocity offsets we have observed of 52–342 km s^{-1}. The 3σ line flux detection limits at each of these 11 locations were then averaged to give an approximate upper limit for the entire wavelength range.

We contend that in light of the discussion put forth above, the SED modelling discussed in this paper has done a reasonable job of matching our observations, but there is still room for improvement. It is possible that attributing some of the model line flux to the Hβ line, instead of solely to the [O III] would provide an even better match between the observed line fluxes and observed [O III] line fluxes. This can be explored in future work and is beyond the scope of this paper. We also assert that additional spectroscopic observations of LAEs in the NIR are needed, yielding both detections and non-detections, to better quantify exactly how successful this approach can be, beyond what we can say with a sample of only six LAEs with [O III] detections/non-detections. Perhaps most importantly, the predictions of [O III] flux that we have made from the new SED fitting approach in this paper should allow us to select the LAEs that are mostly likely to yield [O III] detections in future NIR spectroscopic observations. Based on our comparisons of predicted [O III] line fluxes to observed line fluxes in the three objects that had [O III] detections, it seems likely that objects with strong [O III] line fluxes predicted would be our best bet for NIR follow-up observations. This is a testable hypothesis and should allow us to more efficiently use telescope time and more carefully plan appropriate integration times for each object.

6.2 Effects of including [O III] emission

As has been pointed out by Schaerer & de Barros (2009) and others, inclusion or exclusion of nebular emission lines during SED fitting can significantly alter the results obtained, specifically masses and ages. To investigate how our additional [O III] parameter affects our best-fitting solutions, we compare the best allowed-fit solutions with and without [O III] emission. We focus our discussion here on the three objects for which we have [O III] measurements, and repeat the same fitting procedure described above, but with the [O III] line flux contribution to the K_s band fixed to zero. Unsurprisingly, the object most affected by removing the [O III] parameter is LAE40844. This is unsurprising as this was the LAE with the largest of the three

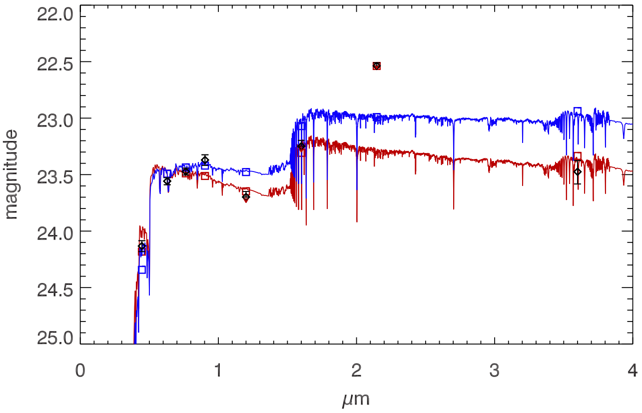

Figure 18. Observed magnitudes are in black. The best allowed-fit solution with an [O III] contribution is shown with red spectrum and red squares, the best-fitting solution with no [O III] line flux is shown with blue spectrum and blue squares. In addition to yielding a more massive solution, the blue spectrum is a much poorer fit.

observed [O III] fluxes, and was also fitted with largest [O III] flux solution among the entire LAE sample. For LAE40844, the best allowed-fit mass increases from $2.2^{+0.0}_{-0.8} \times 10^9$ M$_\odot$ ([O III] included) to $3.5^{+0.05}_{-0.2} \times 10^9$ M$_\odot$ when [O III] emission is not included. So the best allowed-fit mass solution in this object increases 1.6 times when [O III] is not properly accounted for. Perhaps most tellingly, the reduced χ^2 value increases from 9.1 to 145.9 when the [O III] contribution is removed, indicating that the fit without an [O III] contribution is quite poor. This increase in mass is in excellent agreement with those reported in Schaerer & de Barros (2009). Fig. 18 illustrates the difference between the models when [O III] flux is and is not included. LAE27878 and LAE7745 are the other two objects with measured [O III] fluxes. LAE27878 has a very small best allowed-fit [O III] solution, and the results are indistinguishable when [O III] is fixed at 0. The case of LAE7745 is not quite as clear as those of LAE27878 and LAE40844. LAE7745 has a negative best allowed-fit τ parameter when [O III] flux is considered. It has not been previously investigated how age and mass solutions behave when you exclude nebular emission in objects fitted with negative τ value. For this object, we find that when [O III] flux is fixed to zero, the best-allowed fit solution instead chooses a positive τ. Subsequently, the best allowed-fit age and mass in this object decrease, rather than increase (in all comparisons in this section, we are comparing model ages, not star-formation-weighted ages which are dependent on τ). But, in spite of these decreases, the reduced χ^2 value still increases significantly when [O III] is excluded from 12.6 to 33.2.

We present the overall trends for the changes in age, mass, and reduced χ^2 for the entire sample of 33 LAEs in Fig. 19 when [O III] flux is and is not included in the fitting process. The histograms in Fig. 19 present the per cent difference between the solution with [O III] and the solution without [O III]. In all three histograms a positive per cent difference means the solution without [O III] was larger, a negative per cent difference means the solution with [O III] was larger. The two most definitive trends are seen in the histograms for mass and reduced χ^2. Overall, the solutions without [O III] are on average more massive, as seen by the fact that most of the per cent differences in this panel are positive. 19 solutions become more massive, 8 stay the same, and only 6 get less massive. The reduced χ^2 results are even more clear, every χ^2 value gets larger or stays the same, none get smaller. More precisely, 25 solutions get bigger and 8 stay the same. The trend in the age results (model ages, not star-formation-weighted ages) is not quite as definitive, 16 solutions do not change, while 6 get older and 11 get younger. So overall we can say that when [O III] contributions to the K_s band are not included, the sample becomes more massive and less well fit. The magnitude of these effects, however, can vary significantly from object to object within a sample.

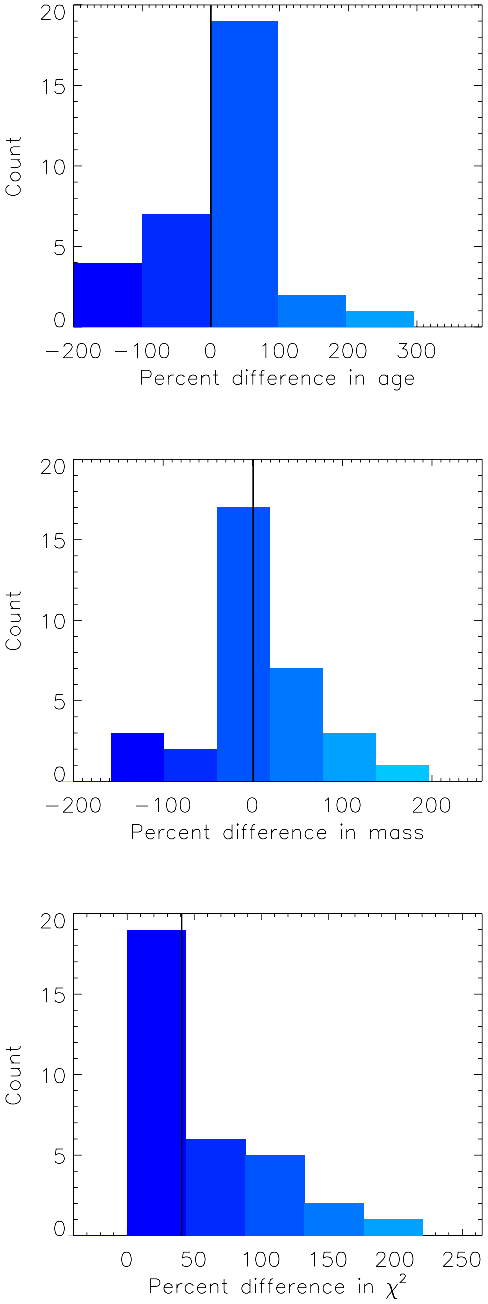

Figure 19. Per cent difference between best allowed-fit solutions in full LAE sample, when [O III] line flux contributions are and are not included in the fitting process. A positive per cent difference means the solution without [O III] was larger, a negative per cent difference means the solution with [O III] was larger. Black vertical line indicates median per cent difference for sample. Overall, when [O III] contributions to the K_s band are not included, the sample becomes more massive and less well fit, even when increasing star formation histories are allowed with some less definitive changes in ages be expected as well – see text for further details.

Table 4. Comparison to SED fitting in the literature. Note that ages presented here are direct model ages, not star-formation-weighted ages for easier comparison to other samples.

Author	Redshift	Sample	Models	Neb. Em.[a]	Results
Acquaviva et al. (2011)	$z \sim 2.1$	216 stacked	CB11	Yes	50 Myr, 3×10^8 $M_\odot$
	$z \sim 3.1$	70 stacked	CB11	Yes	1000 Myr, 1.5×10^9 $M_\odot$
Cowie et al. (2011)	$z \sim 0.3$	40 individual	BC03	Yes	10–10 000 Myr, 10^7–10^{11} $M_\odot$
Finkelstein et al. (2007)	$z \sim 4.5$	98 stacked[b]	BC03	Lyα	1–40 Myr, 0.68–16.2 $\times 10^8$ $M_\odot$
Finkelstein et al. (2009)	$z \sim 4.5$	14 individual	BC03	Lyα, Hα	3–500 Myr, 1.6×10^8–5.0×10^{10} $M_\odot$
Finkelstein et al. (2011a)	$z \sim 0.3$	12 individual	BC07	Yes	60–9000 Myr, 1.1×10^9–3.4×10^{10} $M_\odot$
Gawiser et al. (2006)	$z \sim 3.1$	40 stacked	BC03	No	90 Myr, 5×10^8 $M_\odot$
Gawiser et al. (2007)	$z \sim 3.1$	52 stacked	BC03	No	20 Myr, 1×10^9 $M_\odot$
Guaita et al. (2011)	$z \sim 2.1$	216 stacked	CB10	No	10 Myr, 3.2×10^8 $M_\odot$
Lai et al. (2008)	$z \sim 3.1$	76 stacked	BC03	Only Lyα	160 Myr, 3×10^8 $M_\odot$
This paper	$z \sim 3.1$	33 individual	CB11	Yes, see Section 4	1.5–1800 Myr, 7.1×10^7–6×10^{10} $M_\odot$
Nakajima et al. (2012)[e]	$z \sim 2.2$	304 stacked	BC03	Yes	12.6 Myr, 3×10^8 $M_\odot$
	$z \sim 2.2$	55 stacked	BC03	Yes	8.3 Myr, 5×10^8 $M_\odot$
Nilsson et al. (2007)	$z \sim 3.15$	23 stacked	BC03	No	830 Myr[c], 8×10^8 $M_\odot$
Nilsson et al. (2011)	$z \sim 2.3$	40 stacked	NisseFit[d]	Yes	440 Myr, 2.5×10^{10} $M_\odot$
	$z \sim 2.3$	40 individual	NisseFit[d]	Yes	1000 Myr, 1.7×10^{10} $M_\odot$
Ono et al. (2010a)	$z \sim 3.1$	200 stacked	BC03	No	65 Myr, 1.3×10^8 $M_\odot$
	$z \sim 3.1$	5 individual	BC03	No	4.8–407 Myr, 0.93–27 $\times 10^9$ $M_\odot$
	$z \sim 3.7$	61 stacked	BC03	No	5.8 Myr, 3.2×10^8 $M_\odot$
	$z \sim 3.7$	6 individual	BC03	No	1.4–900 Myr, 3.9–51 $\times 10^9$ $M_\odot$
Ono et al. (2010b)	$z \sim 5.7$	165 stacked	BC03	Yes	3 Myr, 3×10^7 $M_\odot$
	$z \sim 6.6$	91 stacked	BC03	Yes	1 Myr, 1×10^8 $M_\odot$
Pirzkal et al. (2007)	$z \sim 4$–5.7	9 individual	BC03	No	0.5–20 Myr, 5×10^6–18×10^8 $M_\odot$
Vargas et al. (2013)	$z \sim 2.1$	20 individual	BC03	Yes	4–470 Myr, 2.3×10^7–8.5×10^9 $M_\odot$

[a] Was nebular emission accounted for?
[b] Divided into six subsamples.
[c] Author notes this is poorly constrained.
[d] Based on BC03.
[e] Two different stacks for two different fields at $z \sim 2.2$.

6.3 Comparison of physical characteristics to other samples

Table 4 shows best-fitting age and mass results from the majority of recent papers on SED fitting of LAEs from $z \sim 0.3$–6.6, including the results of this paper. We note which models were used in each paper and whether nebular emission lines were included. The reader should also consider that star formation histories and metallicities are sometimes treated differently from paper to paper (i.e. in some cases these are fixed parameters, in others they are free). Focusing specifically on the $z \sim 3.1$ samples detailed in Table 4, we find the results vary substantially from sample to sample. We find that our sample of 33 individually fit LAEs has, on average, a systematically more massive solution than all the stacked samples at $z \sim 3.1$, even in the samples where nebular emission lines were not treated during the fitting process.

There are a number of systematic differences between the samples that may indicate that our results do not necessarily contradict the other works to which we are comparing, but rather we may be probing different subsamples of LAEs. For instance, while our LAEs are spectroscopically confirmed, our selection criteria (Section 2.3 in some cases differ substantially from other authors and this may contribute to some of the differences in derived physical characteristics we have observed. Also, as we alluded to earlier, given the wide-field and correspondingly shallow nature of our NB survey, we have selected a subset of bright LAEs, brighter than many surveys to which we can compare in Table 4. L^* for $z \sim 3.1$ LAEs is $\sim 5.75 \times 10^{42}$ erg s^{-1} (Ciardullo et al. 2012). The majority of our sample is above this luminosity, as illustrated in Fig. 20, where our average $L_{\mathrm{Ly}\alpha}$ luminosity is $\sim 1.50 \times 10^{43}$ erg s^{-1}. This is in contrast, for instance, to the $z \sim 2.1$ and 3.1 LAEs selected from the deep MUSYC survey (Gawiser et al. 2007; Lai et al. 2008; Guaita et al. 2011) where the area surveyed was much smaller but the 5σ NB depth reached magnitudes of 25.4 and 25.1 for $z \sim 3.1$ and $z \sim 2.1$, respectively. We have analysed the effect of $L_{\mathrm{Ly}\alpha}$ on the SED-derived masses in Fig. 20 in a subset of samples from $z \sim 0.3$–3.1 from Table 4 where $L_{\mathrm{Ly}\alpha}$ information readily available. L^* for $z \sim 0.3$ is taken from Cowie, Barger & Hu (2010), and L^* at $z \sim 2.1$ comes from Ciardullo et al. (2012). This preliminary analysis indicates that individually fit LAEs have larger masses than the masses derived from stacked analysis. Also the stacked LAEs from the deeper MUSYC data have smaller masses than those LAEs in our wide-field survey.

We cannot make similarly broad statements about any systematic offset when comparing our age results to the stacked age results at $z \sim 3.1$. Acquaviva et al. (2012) have an older average while Gawiser et al. (2006, 2007) have younger solutions (where both authors stack their samples) than our average from individually fit LAEs. Nilsson et al. (2007) find a solution more than five times older than our average, with constant star formation assumed, but various metallicities allowed. The Acquaviva et al. (2012) fitting procedure assumes constant star formation, but metallicity is allowed to vary; the Gawiser et al. (2006) sample was also fitted with a constant star formation but with metallicity fixed to solar. Gawiser et al. (2007) used a two-burst scenario for their star formation history, and metallicity was allowed to vary. Lai et al. (2008) on the other hand, in spite of being a stacked sample, with no treatment of nebular emission lines, and assuming constant star formation and solar metallicity, finds a very similar average age of 160 Myr compared to our average of 151 Myr. We note, however, that our full range of age solutions (1.1–1100 Myr) does encompass the all the average

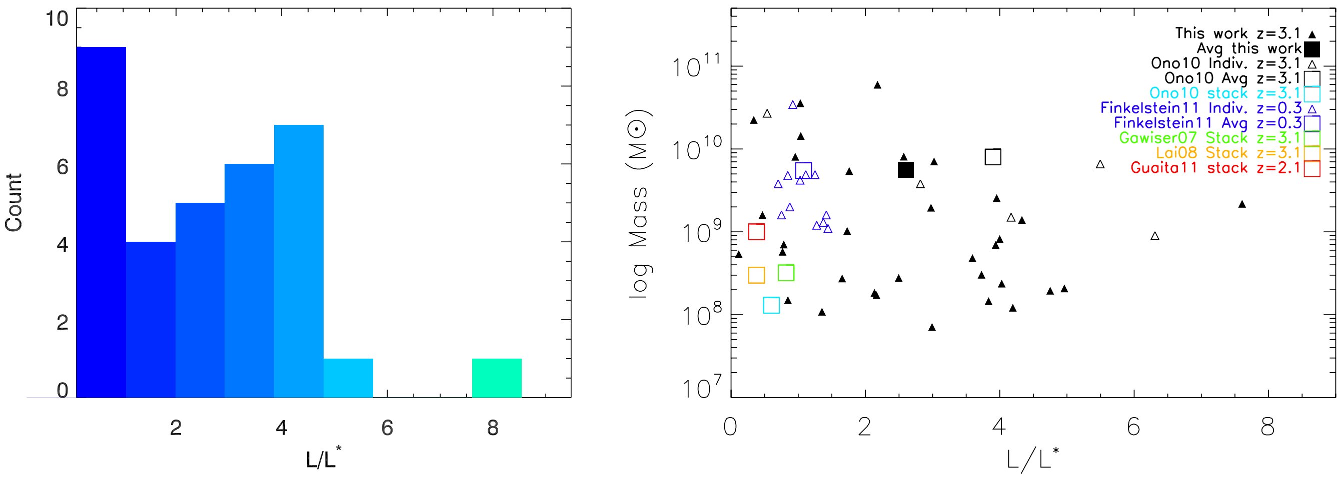

Figure 20. Left shows histogram of L/L^*, where L^* is from Ciardullo et al. (2012). Right shows derived masses as a function of the ratio of L/L^*. Individual results from this paper are shown as small black triangles, an average value from this work is indicated with a large filled black square. 12 individual $z \sim 0.3$ LAEs from Finkelstein et al. (2011a) are shown as blue triangles, a large blue square indicates the average value from this sample. Small open black triangles are five individual $z \sim 3.1$ LAEs from Ono et al. (2010) and the large open black square shows the average value of this sample. The large cyan square is the result from the 200 stacked $z \sim$ LAEs in Ono et al. (2010). The green and orange squares are the same stack of 52 LAEs at $z \sim 3.1$ from Lai et al. (2008) and Gawiser et al. (2007) fitted with different star formation histories. The red square is the stack of 216 $z \sim 2.1$ LAEs from Guaita et al. (2011).

ages put forth by other authors for their stacked samples. We acknowledge that the variety of methods used by different authors can make direct comparison somewhat difficult, but it is worth trying to catalogue the various results and compare to the extent we are able.

Ono et al. (2010) presents the only other sample of individually fit LAEs at $z \sim 3.1$, albeit in a sample of only five objects, to which we can compare. The fitting procedure of Ono et al. (2010) includes an assumed metallicity of $Z = 0.2\,\mathrm{Z}_{\odot}$ the star formation history can be constant or decreasing exponentially, and no treatment of nebular lines is included. In spite of these differences, we find good agreement between their ranges for both mass and age, and those that we have presented for our sample. They find (as we do) a large range of ages, 4.8–407 Myr (1.5–1800 Myr), and masses, 9.3×10^{8}–$2.7 \times 10^{10}\,\mathrm{M}_{\odot}$ (7.1×10^{7}–$6 \times 10^{10}\,\mathrm{M}_{\odot}$). The fact that this individually fit sample is the only one that matches our results well may lend further credence to the idea that stacked analyses may not be capturing the diversity that we have found in the LAE population at this redshift. While Vargas et al. (2013) find a moderately diverse sample of properties in their 20 individually fit $z \sim 2.1$ LAEs, the spread we find in both our age and mass results are significantly larger. We also note that there is broad agreement between our individually fit LAEs at $z \sim 3.1$ and the 40 individually fit LAEs of Cowie et al. (2011) at $z \sim 0.3$ and 12 individually fit LAEs from Finkelstein et al. (2011a). The age and mass spread of the samples is quite similar, except, of course, the fact that there are older possible ages allowed for galaxies in the $z \sim 0.3$ Universe compared to the $z \sim 3.1$ Universe. Such agreement between samples far removed from one another in cosmic time could suggest that Lyα selection techniques are capturing similar objects, at similar states of evolution, regardless of the redshift sampled. The broad agreement may also be a result of the similar $L_{\mathrm{Ly}\alpha}$ space probed by the $z \sim 0.3$ sample and our sample, as the $z \sim 0.3$ sample has a rather large average L/L^* value of ~ 1.6 (using L^* from Cowie et al. 2010).

7 CONCLUSIONS

We have presented one new [O III] detection in a $z \sim 3.1$ LAE. Combining this new detection with the two we presented in Mc11, we are able to present a total of three measurements of the velocity offset between Lyα and [O III] in these $z \sim 3.1$ LAEs, ranging from 52 to 342 km s^{-1}. This new result is still consistent with the outflow models explored in Mc11.

In addition to the new [O III] detection, we have put forth a simple method to account for nebular emission in high-z starbursting galaxies, motivated by our three [O III] measurements. We have individually fit 33 $z \sim 3.1$ LAEs using this powerful yet simple method to account for nebular emission line contributions to galaxy SEDs. From these fits, we find constraints on age, mass, dust content, metallicity, star formation history, and [O III] line flux. We find that our sample has quite diverse characteristics, but some generalizations can be made. For instance, a majority of the galaxies are fitted with a single instantaneous burst or exponentially decreasing star formation history. As a whole, the sample has only moderate amounts of dust, and subsolar metallicity. Mass and age solutions vary widely, but median values of 4.5×10^{6} yr (full range is 1.4×10^{6}–4.6×10^{8} yr) and $6.9 \times 10^{8}\,\mathrm{M}_{\odot}$ (full range is 7.1×10^{7}–$6 \times 10^{10}\,\mathrm{M}_{\odot}$) are found. Finally, most of the galaxies are best fitted with an [O III] line contributing additional flux to the K_s band, with an average flux of 7.3×10^{-17} erg s^{-1} cm^{-2} (or an average of 9.7×10^{-17} erg s^{-1} cm^{-2} among the 25 galaxies with non-zero line flux solutions, ranging from 7.0×10^{-18} to 3.7×10^{-16} erg s^{-1} cm^{-2}).

The [O III] line strength predictions from our new SED fitting methodology have reasonably matched the observations of the [O III] line in the six objects for which we can make this comparison. These predictions gives us confidence that these results can be used to select the LAEs mostly likely to yield [O III] detections in future NIR observations and aids in planning adequate integration times for the most efficient use of such future NIR observing time. Further observations of LAEs in the NIR will allow us to fill in the distribution of velocity offsets found in LAEs at this redshift, and will allow us to further test the validity of [O III] line strength predictions from our SED fitting process. In the meantime, we have, with this work, provided a comprehensive picture of LAE characteristics in a large sample of individually examined objects.

ACKNOWLEDGEMENTS

We thank NOAO for loaning the KPNO [O III] filter for use on the Bok Telescope. This work has been supported by NASA (programme N067NS), and by the National Science Foundation through NSF grant AST-0808165. Additional thanks to Dr Seth Cohen for many helpful discussions.

Some of the data presented herein were obtained at the W. M. Keck Observatory, which is operated as a scientific partnership among the California Institute of Technology, the University of California, and the National Aeronautics and Space Administration. The Observatory was made possible by the generous financial support of the W. M. Keck Foundation.

The LBT is an international collaboration among institutions in the US, Italy, and Germany. LBT Corporation partners are The University of Arizona on behalf of the Arizona university system; Instituto Nazionale di Astrofisica, Italy; LBT Beteiligungsgesellschaft, Germany, representing the Max-Planck Society, the Astrophysical Institute Potsdam, and Heidelberg University; The Ohio State University, and The Research Corporation, on behalf of The University of Notre Dame, University of Minnesota, and University of Virginia.

Observations reported here were obtained at the MMT Observatory, a joint facility of The University of Arizona and the Smithsonian Institution.

The authors wish to recognize and acknowledge the very significant cultural role and reverence that the summit of Mauna Kea has always had within the indigenous Hawaiian community. We are most fortunate to have the opportunity to conduct observations from this mountain.

REFERENCES

Acquaviva V., Vargas C., Gawiser E., Guaita L., 2011, ApJ, 751, L26
Acquaviva V., Vargas C., Gawiser E., Guaita L., 2012, ApJ, 751, L26
Ageorges N. et al., 2010, in McLean I. S., Ramsay S. K., Takami H., Proc. SPIE Conf. Ser. Vol. 7735, Ground-Based and Airborne Instrumentation for Astronomy III. SPIE, Bellingham, p. 77351L
Becker G. D., Sargent W. L. W., Rauch M., Simcoe R. A., 2006, ApJ, 640, 69
Bertin E., Arnouts S., 1996, A&AS, 117, 393
Boulade O. et al., 2003, in Iye M., Moorwood A. F. M., eds, Proc. SPIE Conf. Ser. Vol. 4841, Instrument Design and Performance for Optical/Infrared Ground-Based Telescopes. SPIE, Bellingham, p. 72
Bruzual G., Charlot S., 2003, MNRAS, 344, 1000
Calzetti D., Armus L., Bohlin R. C., Kinney A. L., Koornneef J., Storchi-Bergmann T., 2000, ApJ, 533, 682
Capak P. et al., 2007, ApJS, 172, 99
Chonis T. S. et al., 2013, ApJ, 775, 99
Ciardullo R. et al., 2012, ApJ, 744, 110
Cowie L. L., Hu E. M., 1998, AJ, 115, 1319
Cowie L. L., Barger A. J., Hu E. M., 2010, ApJ, 711, 928
Cowie L. L., Barger A. J., Hu E. M., 2011, ApJ, 738, 136
Dawson S. et al., 2004, ApJ, 617, 707
Elvis M. et al., 2009, ApJS, 184, 158
Fabricant D. et al., 2005, PASP, 117, 1411
Finkelstein S. L., Rhoads J. E., Malhotra S., Pirzkal N., Wang J., 2007, ApJ, 660, 1023
Finkelstein S. L., Rhoads J. E., Malhotra S., Grogin N., Wang J., 2008, ApJ, 678, 655
Finkelstein S. L., Rhoads J. E., Malhotra S., Grogin N., 2009, ApJ, 691, 465
Finkelstein S. L., Cohen S. H., Moustakas J., Malhotra S., Rhoads J. E., Papovich C., 2011a, ApJ, 733, 117
Finkelstein S. L. et al., 2011b, ApJ, 729, 140
Finlator K., Oppenheimer B. D., Davé R., 2011, MNRAS, 410, 1703
Fukugita M., Yasuda N., Doi M., Gunn J. E., York D. G., 2011, AJ, 141, 47
Gawiser E. et al., 2006, ApJ, 642, L13
Gawiser E. et al., 2007, ApJ, 671, 278
Guaita L. et al., 2011, ApJ, 733, 114
Kashikawa N. et al., 2006, ApJ, 648, 7
Kelson D. D., 2003, PASP, 115, 688
Koekemoer A. M. et al., 2007, ApJS, 172, 196
Kulas K. R., Shapley A. E., Kollmeier J. A., Zheng Z., Steidel C. C., Hainline K. N., 2012, ApJ, 745, 33
Lai K., Huang J.-S., Fazio G., Cowie L. L., Hu E. M., Kakazu Y., 2007, ApJ, 655, 704
Lai K. et al., 2008, ApJ, 674, 70
Leauthaud A. et al., 2007, ApJS, 172, 219
Madau P., 1995, ApJ, 441, 18
Malhotra S., Rhoads J. E., 2002, ApJ, 565, L71
Malhotra S., Rhoads J. E., 2004, ApJ, 617, L5
Malhotra S., Rhoads J. E., Finkelstein S. L., Hathi N., Nilsson K., McLinden E., Pirzkal N., 2012, ApJ, 750, L36
Maraston C., Pforr J., Renzini A., Daddi E., Dickinson M., Cimatti A., Tonini C., 2010, MNRAS, 407, 830
Massey R., Stoughton C., Leauthaud A., Rhodes J., Koekemoer A., Ellis R., Shaghoulian E., 2010, MNRAS, 401, 371
McCracken H. J. et al., 2010, ApJ, 708, 202
McCracken H. J. et al., 2012, A&A, 544, A156
McLean I. S. et al., 1998, in Fowler A. M., ed., Proc. SPIE Conf. Ser. Vol. 3354, Infrared Astronomical Instrumentation. SPIE, Bellingham, p. 566
McLinden E. M. et al., 2011, ApJ, 730, 136 (Mc11)
Monet D. G. et al., 2003, AJ, 125, 984
Nakajima K. et al., 2012, ApJ, 745, 12
Nakajima K., Ouchi M., Shimasaku K., Hashimoto T., Ono Y., Lee J. C., 2013, ApJ, 769, 3
Nilsson K. K. et al., 2007, A&A, 471, 71
Nilsson K. K., Östlin G., Møller P., Möller-Nilsson O., Tapken C., Freudling W., Fynbo J. P. U., 2011, A&A, 529, A9
Ono Y. et al., 2010a, MNRAS, 402, 1580
Ono Y., Ouchi M., Shimasaku K., Dunlop J., Farrah D., McLure R., Okumura S., 2010b, ApJ, 721, 1524
Ouchi M. et al., 2003, ApJ, 582, 60
Ouchi M. et al., 2008, ApJS, 176, 301
Papovich C., Dickinson M., Ferguson H. C., 2001, ApJ, 559, 620
Papovich C. et al., 2006, AJ, 132, 231
Papovich C., Finkelstein S. L., Ferguson H. C., Lotz J. M., Giavalisco M., 2011, MNRAS, 412, 1123
Pickles A. J., 1998, PASP, 110, 863
Pirzkal N., Malhotra S., Rhoads J. E., Xu C., 2007, ApJ, 667, 49
Raichoor A. et al., 2011, ApJ, 732, 12
Rhoads J. E., Malhotra S., 2001, ApJ, 563, L5
Rhoads J. E., Malhotra S., Stern D., Wang J., Dey A., Spinrad H., Jannuzi B. T., 2000, ApJ, 671, 1227
Rhoads J. E. et al., 2003, AJ, 125, 1006
Sanders D. B. et al., 2007, ApJS, 172, 86
Schaerer D., de Barros S., 2009, A&A, 502, 423
Seifert W. et al., 2003, in Iye M., Moorwood A. F. M., eds, Proc. SPIE Conf. Ser. Vol. 4841, Instrument Design and Performance for Optical/Infrared Ground-Based Telescopes. SPIE, Bellingham, p. 962
Spergel D. N. et al., 2007, ApJS, 170, 377
Steidel C. C., Erb D. K., Shapley A. E., Pettini M., Reddy N., Bogosavljević M., Rudie G. C., Rakic O., 2010, ApJ, 717, 289
Valdes F., 1993, Guide to the Kitt Peak Coude Slit Reduction Task DOSLIT. Central Computer Services, NOAO
Vargas C. J. et al., 2013, preprint (arXiv:e-prints)
Verhamme A., Schaerer D., Maselli A., 2006, A&A, 460, 397
Verhamme A., Schaerer D., Atek H., Tapken C., 2008, A&A, 491, 89
Williams G. G., Olszewski E., Lesser M. P., Burge J. H., 2004, in Moorwood A. F. M., Iye M., eds, Proc. SPIE Conf. Ser. Vol. 5492, Ground-Based Instrumentation for Astronomy. SPIE, Belligham, p. 787

Wright E. L., 2006, PASP, 118, 1711

Zheng Z. Y., Wang J. X., Finkelstein S. L., Malhotra S., Rhoads J. E., Finkelstein K. D., 2010, ApJ, 718, 52

SUPPORTING INFORMATION

Additional Supporting Information may be found in the online version of this article:

APPENDIX A: ADDITIONAL FIGURES (http://mnras.oxfordjournals.org/lookup/suppl/doi:10.1093/mnras/stu023/-/DC1).

This paper has been typeset from a TEX/LATEX file prepared by the author.